THE ROLE OF DAMAGE CASCADE

IN THE NANOCRYSTALLIZATION OF METALLIC GLASS

A Thesis

by

MICHAEL THOMAS MYERS

Submitted to the Office of Graduate Studies of
Texas A&M University
in partial fulfillment of the requirements for the degree of

MASTER OF SCIENCE

May 2010

Major Subject: Nuclear Engineering

THE ROLE OF DAMAGE CASCADE

IN THE NANOCRYSTALLIZATION OF METALLIC GLASS

A Thesis

by

MICHAEL THOMAS MYERS

Submitted to the Office of Graduate Studies of
Texas A&M University
in partial fulfillment of the requirements for the degree of

MASTER OF SCIENCE

Approved by:

Chair of Committee,   Lin Shao
Committee Members,   Sean McDeavitt
                                    Xhinghang Zhang
Head of Department,   Raymond Juzaitis

May 2010

Major Subject: Nuclear Engineering

ABSTRACT

The Role of Damage Cascade

in the Nanocrystallization of Metallic Glass. (May 2010)

Michael Thomas Myers, B.S., The Ohio State University

Chair of Advisory Committee: Dr. Lin Shao

The Multi-scale modeling of ion-solid interactions presented can lead to a fundamentally new approach for understanding temperature evolution and damage formation. A coupling of the Monte Carlo code, SRIM, to a C++ FEM heat transfer code was performed, enabling a link between the damage cascade event to the subsequent heat transfer. Modeling results indicate that for 1 MeV Ni$^+$ ion irradiation in $Ni_{52.5}Nb_{10}Zr_{15}Ti_{15}Pt_{7.5}$, the heat transfer rate is too large for direct crystallization. Although the damage cascade induces a peak temperature of 5300 K, within 6 picoseconds the temperature is below the glass transition temperature. This result implies that there is a cooling rate of 10^{14} K/s, which is much greater than the critical cooling rate for this material. Ion irradiation was performed to compare modeling with experiment. No evidence of direct crystallization is observed under TEM. Nanocrystals are formed as a consequence of series of multistage phase transitions. This provides evidence that the energy dissipation occurs too quickly for direct crystallization, as crystals are found in regions having undergone substantial compositional changes. A host of conventional electron microscopy methods were employed to characterize the structural changes induced by 1 MeV Ni$^+$ ion irradiation in $Ni_{52.5}Nb_{10}Zr_{15}Ti_{15}Pt_{7.5}$ and identify the phases that form, Ni_3Nb, Ni_3Ti and Ni_3Zr. Scanning TEM analysis revealed Pt segregation near crystal regions due to irradiation. Due to a lack of Pt crystal phases observed and high concentrations of Pt in crystal regions it is postulated that Pt is substituting for Ni to form $(Ni,Pt)_3Nb$ and $(Ni,Pt)_3Ti$.

To my parents and my wife

ACKNOWLEDGMENTS

I would like to acknowledge Dr. Lin Shao for his encouragement during my time at Texas A&M. His discussions are always insightful, thought provoking and invaluable to me. Dr. Shao's expertise in the field of ion-solid interactions is something that I do not take for granted and I appreciate the time he has afforded me in this learning process.

I would like to thank my committee members, Dr. Sean McDeavitt and Dr. Xinghang Zhang for their support over the course of the present work.

I acknowledge our collaborators Dr. Xuemei Wang and Dr. Wei-Kan Chu who were instrumental in sample irradiation. A very deep debt of gratitude is owed to Dr. Engang Fu whose patience seemed unlimited while he not only assisted, but took a guiding role in teaching me sample preparation and characterization. I also express a special gratitude to Michael Martin, Jesse Carter, Assel Aitkaliveya, Di Chen and Mark Hollander who have helped me integrate into an experimental environment.

TABLE OF CONTENTS

CHAPTER   Page

LIST OF TABLES

LIST OF FIGURES

FIGURE   Page

CHAPTER I

INTRODUCTION

The discovery of amorphous alloys, otherwise known as metallic glasses (MG), has prompted much research into the behavior and characteristics of this material. It was the group of Klement et al. at the California Institute of Technology which first reported on the production of amorphous alloys in 1960 [1]. The method of production for MG involves rapidly quenching a molten alloy mixture, avoiding crystallization, and ending in an amorphous state. During this process, extremely high critical cooling rates were initially required, limiting the size and geometry to permit such cooling rates. The race was on to find alloys which exhibit a high glass forming ability and could be produced at much lower critical cooling rates. One particular group at Tohoku University has been very successful in their approach and has been able to produce a host of amorphous alloys which have critical cooling rates similar to that of oxide glass [2].

In traditional alloys, there exists a regular, periodic structure which defines the material. MG lacks such long range order and exists in an entirely amorphous state. The final state is characterized as a "metastable state", meaning that if enough energy is supplied to the material, the lowest energy configuration of the system will prevail and the material will revert to the crystalline structure which minimizes the free energy of the system. One example is the first MG produced, which was unstable such that after a prolonged period of time the lowest energy crystalline state would form. Therefore there is a strong desire to produce MG which have a large supercooled liquid region against crystallization, or in other words, is able to freely

—————

The journal model is *IEEE Transactions on Automatic Control.*

accept a large fraction of energy without reverting to the crystal structure. Many MG have exhibited this behavior on a small scale, but recently one alloy in particular has been demonstrated to be particularly stable against crystallization [3].

In typical crystal alloys, grain boundaries are both the source of the materials greatest strength as well as their weakest link. The grain boundaries have high interfacial energy which is able to inhibit the movement of dislocations, effectively giving rise to the strength of the material. It is this "slowing" of dislocations that stops the material from failing catastrophically under an applied stress. Instead of immediate fracture under applied load, the material is able to plastically deform as the dislocations move along the slip plane, encounter a grain boundary, and this boundary acts to resist further motion. The high interfacial energy associated with the grain boundary also makes them centers for diffusion and trapping sites for point defects. It is this type of behavior that leads to cracking, corrosion, creep and limits the useful lifetime of a material.

The amorphous structure of MG necessarily means that it is devoid of defects and also grain boundaries. This fact is particularly useful in that a lack of grain boundaries implies no centers for diffusional segregation and corrosion. There has been a lot of work published regarding the superior properties of MG [4, 5, 6, 7, 8, 9]. But, as is the case with traditional alloys, the greatest strength is also the greatest weakness. Unlike in traditional alloys under an applied load, where the stress is nearly uniformly distributed throughout the entire crystal structure, in MG it is rather nonuniform. The applied stress in the MG takes the form of a small, highly localized shear banding regions. Once the shear band forms, there is simply nothing to deflect the shear bands and stop them from quickly propagating through the entire material under continued applied load. This presents itself in the fact that MG has a tendency to fail after only a few percent strain in a brittle fashion [10, 11]. Work persists to develop amorphous

alloys with higher ductility [12].

In order to arrest the shear band propagation and increase the ductility of MGs, many bulk methods have been proposed to introduce dispersed nanostructures throughout the specimen, including nanoindentation [13], deformation [14], bending [15] and annealing [16]. These efforts have produced nanocomposite MGs with increased mechanical properties which are unachievable by conventional glassy alloys. Other methods, such as electron irradiation [17, 18, 19, 20] and ion irradiation [21, 22, 23] have produced structural changes in MG which have the distinct advantage of being highly localizable as well as controllable.

Thus, the ability of an ion irradiation technique to introduce nanostructures (nanocrystals) into MG, while retaining a large amorphous fraction is very attractive. The reason? Ion irradiation provides the ability to atomistically control the amount of energy that is supplied to the system through the mass and kinetic energy of the implanting species, the desired flux level and finally the overall number of implanted ions. Therefore the study of ion implanted nanocrystal-dispersed MG is of high importance due to the potential wide range of application, but also due to the underlying fundamental physics.

The ion irradiation induced phase transformation process in the amorphous to crystalline phase transformation is not well understood and a number of competing, incomplete theories prevail. Understanding the damage cascade formation and growth is paramount to understand the kinetics of crystallization and solidifying an accurate picture. As it stands, the model of damage cascade in MG can be viewed in the realm of either thermal spike theory [24] or that of the free volume approach of Cohen [25].

When energetic ions slow via stopping in a solid, the kinetic energy of the incoming ion is transferred to the the medium through elastic collisions. Target atoms can then recoil, which can then in turn impart some of their energy to another target,

and so on. This is the basis of a damage cascade. Put very simply, the thermal spike model postulates that surrounding the damage cascade site, there exists a liquid-like hot zone that is partially molten. This results in a region that is considered to be locally melted for a very short period of time, which quickly solidifies to the solid state. In the case of amorphous metals this implies a direct crystallization method, meaning that one damage cascade would result in enough energy being supplied to the system such that a crystal would persist as the end state.

In the free volume model, atomic diffusion is a function of atomistic jumping from one site to another. The probability of an atom being able to make a transition from one site to another is determined by the amount of available volume for that atom in its new location and the relative frequency at which it tries to make the jump. It is this idea that encompasses a diffusion coefficient based on the ability to find a volume large enough to occupy the transitioning atom and the jump being energetically favorable. If there is not enough free volume, the atom is essentially bound in a cage which is defined by the nearest neighbors. In the case of ion irradiation, the damage cascade, or a series of overlapping cascades is able to provide enough energy and volume enhancement in small regions such that crystallization at particular sites can occur indirectly, as a culmination of small steps.

As previously stated, the damage cascade plays a vital role in understanding the phase transformation of MG under ion irradiation. Understanding the physics behind the crystallization behavior of MG relies on the ability to accurately model the role of thermal spike in the material as well as perform experimental verification. It is the aim of the current thesis to therefore model and predict the role of damage cascades in amorphous metals. In order to achieve this goal, modeling will be linked with experiment to allow predictions of crystallization behavior in future novel amorphous alloys.

Modeling will provide the temperature distributions which are experienced after the damage cascade has formed. For a given damage cascade, the amount of time that it takes for the cascading collisions to stop is on the order of one picosecond. Therefore, the primary focus will be on the subsequent time evolution of the temperature profiles inside the MG after the initial cascade. The 2-D and 3-D temperature profiles generated will be used to predict the ability for crystal phase formation under ion irradiation. This will aid in understanding the role that ion irradiation induced temperature changes have on the crystallization behavior.

Following the initial modeling, ion irradiation will be used to experimentally characterize the role of damage cascade in crystal formation. Heavy ion irradiation will produce structural changes which can be observed and characterized using traditional transmission electron microscopy (TEM) methods. TEM and various other methods will be used to observe the crystallization behavior and determine whether crystallization is direct or indirect, as well as determine the phases that persist and finally determine the final composition changes.

To produce 2-D and 3-D temperature profiles due to ion-solid interactions, a coupling was performed between the current Monte Carlo code SRIM [26] and a Finite Element Method (FEM) [27] heat transfer code written for this purpose (see Apendix A). The SRIM code is frequently used for calculating damage profiles and allows the user to input a myriad of species and energies to produce damage cascades, ideal for the current situation. For this study, a single damage cascade calculation was performed using the SRIM code, whose output contains the positions and kinetic energies of the recoil atoms inside the material. The kinetic energy is directly related to the temperature and can thus be used as a point temperature source in a heat transfer code.

The development of a FEM C++ heat transfer code was completed, with the

ability to input the aforementioned heat sources as initial conditions. The code was developed using the "dealii" libraries [27] currently under development in part by researchers at Texas A&M University. The code allows for linear as well as higher order polynomial elements on unstructured meshes of arbitrary geometry. The solution engine employs a Crank-Nicholson numerical scheme to solve for temperature profiles with a conjugate-gradient (CG) convergence control. The code implements the appropriate initial and boundary conditions, using actual thermal diffusivity, specific heat and material density to visually depict the temperature evolution as a function of time.

The experimental portion involves the use of a novel MG, namely $Ni_{52.5}Nb_{10}Zr_{15}Ti_{15}Pt_{7.5}$. The MG is irradiated using an NEC 1.7 MeV tandem accelerator at a beam current of 160 nA cm^{-2} to a fluence of 1x10^{16} cm^{-2} with 1 MeV Ni$^+$ ions. Following irradiation, the samples were analyzed for compositional changes using X-ray diffraction (XRD), transmission electron microscopy (TEM), high-resolution TEM as well as scanning TEM (STEM). All TEM specimen were prepared conventionally and final polishing was achieved by room temperature 2 keV Ar ion milling with continuous rocking to ensure homogenous etching. By characterizing the final composition, crystal formation and concentration changes, an investigation is performed to deduce whether the crystallization method was that of direct or indirect processes as a result of the damage cascade.

CHAPTER II

ION-SOLID INTERACTIONS

The following chapter will explain the physical description of ion-solid interactions. A solid fundamental understanding of ion-solid interactions is necessary to be able to develop multi-scale modeling and perform experimental verification of those models.

The topic of ion-solid interactions is very broad and encompasses a wide range of theories and applications. The use of ion beams takes many forms, from ion implantation, ion mixing, doping, surface modification, material characterization and many others. The bombardment of foreign atoms into a substrate also has the ability to change material properties such as the mechanical, electrical, thermal and optical characteristics.

A. Ion Acceleration

In most ion-solid interactions, the incident ions are produced using an ion source and are accelerated through an electric potential, otherwise known as an acceleration column. Mass separation is achieved using a magnetic field to steer only the desirable ion species towards the target chamber. To focus the beam, electrostatic or magnetic lenses are employed. The beam is then rastered over the desired area using a technique, known as beam sweeping, which uses magnetic fields to steer the beam. Although many other forms and variations of accelerators exist, this is presumably the easiest to conceptually illustrate and depicts the basic components of the acceleration system experimentally employed in this work. A schematlic of a typical accelerator is found in Figure 1, taken from [28].

The entire system is held under near vacuum, typically less than 10^{-7} torr, to ensure that there are no ion-gas collisions inside the system. These types of collisions
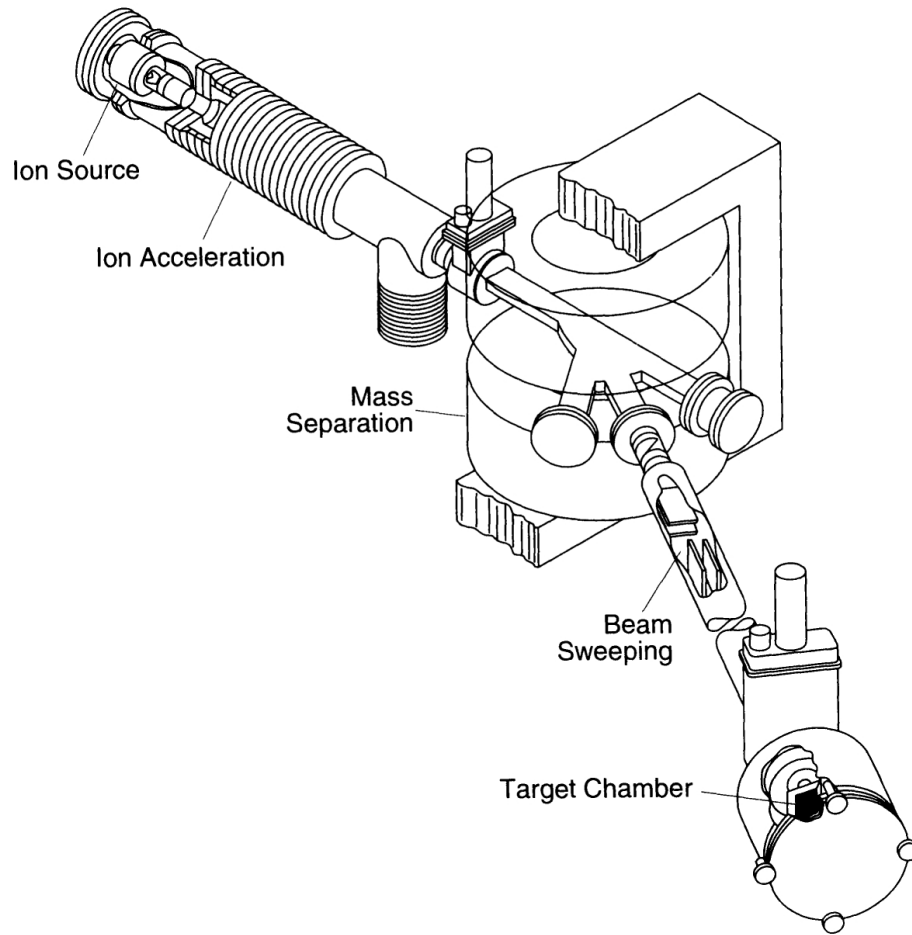
Fig. 1. A schematic of a typical ion acceleration system.

would result in ion energy loss, therefore limiting the ability to definitively know what energy the incident ion carries as it approached the target. Assuming near vacuum conditions, the beam will arrive at the target chamber as a current of ions of the same species and energy. The intensity of the beam is measured in SI units of amperes per square centimeter (A/cm^2) and typical values, depending on the acceleration potential, can range from 10^{-3} to 10^{-6} A/cm^2.

The energy (kinetic energy) of the bombarding ion is dictated by the charge state of the ion and the accelerating potential. To describe this energy, the unit

of electron volt (eV) is used, which is defined as the kinetic energy of a particle accelerated through a potential of one volt with the charge e, where e is the charge of an electron. The SI unit of charge is the coulomb (C) and the charge of an electron is 1.602×10^{-19} C. In the usual way, the known kinetic energy can be used to determine ion velocities such that, $E = \frac{1}{2}mv^2$, where E is the kinetic energy, m is the mass of the ion, and v is the velocity. Typical values of ion energy are on the order of keV (10^6 eV) to MeV (10^9 eV).

The total fluence, Φ is then defined as the normalized number of ions implanted per area. This can be calculated from the beam intensity ϕ, as

$$\Phi = \int \phi \, dt \tag{2.1}$$

using the conversion from amperes to ions per second: $1 \text{ A} = 1 \text{ C/s} = (1.602 \times 10^{-19} \times n)^{-1}$ ion/s, where n is the charge state of the ion.

B. Interactions Between Ions and Atoms

As ions penetrate the target, they make collisions with target atoms in the sample, creating primary knock on atoms (PKA), which in turn have subsequent interactions. All collisions between ions and atoms, and atoms-atoms can be described through the use of interactomic potentials. Understanding the forces at work which dictate momentum and energy transfer are essential to determining ion range, damage creation and concentration.

1.   Interatomic Potentials

The simplest potential model one can envision between two point sources, separated by a distance r is the Coulomb potential, given by

$$V(r) = \frac{e2}{r}. \tag{2.2}$$

In the case of atoms, there exists a positively charges core surrounded by an electron cloud and this simplistic model will not hold as it does not account for this fact. On the other extreme is the hard sphere model, where atoms are treated like billiard balls allowed to make strictly elastic collisions. This also is known not to be the case, electron shells of two colliding atoms can overlap and have significant contributions to the force. The Born-Mayer potential was introduced to account for the overlap of the valence shell electrons as the two are brought nearer. The Born-Mayer potential is given by

$$V(r) = A \, exp(\frac{-r}{B}) \tag{2.3}$$

where the constants A and B are determined experimentally.

At distances much less than the Bohr radius, the Coulomb interaction will be dominate as the repulsive ion cores will be the primary forces. At distances on the order of the equilibrium separation distance, between the two, the Born-Mayer potential will most accurately resolve the forces between two atoms [29].

To account for electronic screening in the region just outside the Bohr radius, a screened Coulomb potential can be used, taking the following form.

$$V(r) = \left(\frac{Z_1 Z_2 e^2}{r}\right) exp(\frac{-r}{a}) \tag{2.4}$$

where Z_1, Z_2 are the atomic masses, and $a = 0.8853 \, a_0 / (Z_1 Z_2)^{1/6}$ and a_0 is the Bohr radius.

A combination of the Born-Mayer potential and the screened Coulomb potential, each accounting for their respective regimes of dominance are a good first approximation to the interatomic potential between two approaching atoms. Two other approaches for calculating interatomic potential are that of Frisov and also Thomas-Fermi-Dirac potentials (TFD). The approach used by Frisov accounts for the mutual approach of the nuclei and therefore accounts for changes in electron energy, very similar to that of screened Coulomb with a different functional form to the screening factor. The Thomas-Fermi-Dirac potential takes into consideration that fact that the electron cloud has a finite spatial distribution and density.

Up to this point, small changes to the screening function had been suggested by Bohr, Lindhard and Frisov, but all were based on simple interatomic potentials. In an attempt to model all interatomic potentials using a single analytical form, Ziegler, Biersack and Littmark performed detailed calculations for 261 atom pairs to find a suitable potential [28]. They were able to derive what is known as the universal screening function together with their ZBL potential model to fit the data. This model is widely used for calculations involving interatomic potentials.

2. Scattering

For the following discussion of elastic scattering, collisions are assumed to be violent collisions, that is they are two body collisions. The particles are treated classically, with electron excitation only impacting the energy loss and not the collision dynamics. In this type of collision one atom is considered to be initially at rest. The problem is now to solve the equations of conservation of energy and momentum for two body collisions. Through these conservation equations, one can determine the energy transfer, momentum transfer and the scattering angle, typically working in the center of mass (CM) frame, due to it's ease of use. In the CM frame, the scattering angle

will depend on the the choice of interatomic potential, the ion energy and the impact parameter. Figure 2 depicts the parameters involved in CM scattering,
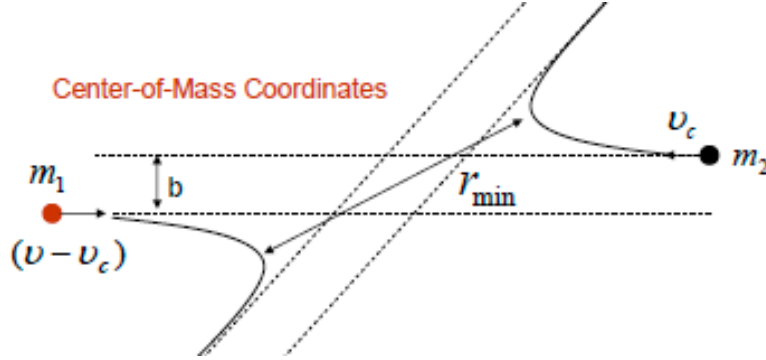
Fig. 2. An illustration of a scattering event as experienced by the projectile and target in the center of mass coordinates.

where v_c is the center of mass velocity, v is the projectile velocity, b is the impact paramter and r_{min} is the line of closest approach. The impact parameter can be thought of as the distance offset from the central force between the two bodies and placing assumptions on this value is critical in solving the classical scattering integral for energy loss and naturally leads to two distinct cases. Bohr proposed their exists two distinct regimes of energy loss due to elastic collisions, one is the nuclear regime where the interaction is purely Coulombic with no screening, i.e. nucleus-nucleus collisions. The other is the electronic regime where he uses the harmonic oscillator model based on interaction frequencies between the electron and the potential to place a cutoff value on the impact parameter. This leads directly into the two main modes of energy transfer and stopping in solids.

3.   Ion Stopping

As an incident ion traverses through a material, the target atoms inside undergo many collisions with a given ion. The path that the ion takes, depends on the crystal

structure, energy and angle of incidence and is by nature complicated. If the target is considered to be a random collection of atoms with no structure, then the ion track can be considered as a series of random scattering events that takes the ion in all directions. The total distance traversed by the particle is given by the range, R,

$$R = \int_{E_0}^{0} \frac{1}{dE/dx} dE, \tag{2.5}$$

where E_0 is the initial energy, and dE/dx represents the energy loss per distance traveled. The more usual quantity for ion implantation is the projected range R_p. This can be described as follows. Given a series of track histories it is unlikely that any two will be identical, but the average perpendicular distance from the surface that an ion travels converges. This can be given as the particles projected range.

The projected range will follow a Gaussian distribution given the assumption of random collisions. Another term, called range straggling, dR_p, is often used to characterize the spread in the range distribution. The range and straggling depend on the details of the problem and the particular stopping mechanism. Projected range values are well tabulated and are the topic of many software simulations such as SRIM [26].

When an energetic ion is incident on a target of many atoms, it slows through collisions described above with target atoms. This process is known as stopping, and can be thought of as two interactions: interactions with target electrons and interactions with target nuclei, electronic and nuclear stopping respectively. A depiction of the energy loss mechanisms is seen in Figure 3.

The nuclear stopping mechanism is dominant for low velocity projectiles, whereas electronic stopping is dominant for high velocity projectiles. Each mechanism is highly dependent on relevant parameters such as the mass, atomic number, and ion velocity. The relationship that exists for particle velocity and the dominant stopping
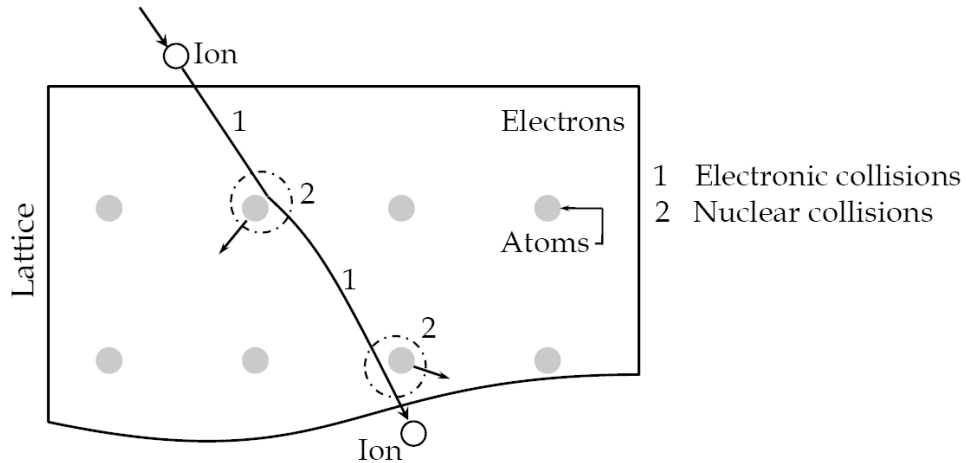
Fig. 3.   A diagrammatic representation of electronic and nuclear collisions between an incident ion and target atoms.

mechanism is depicted in Figure 4.

Due to the nature of the two distinct regimes of ion stopping, it is therefore broken up into it's two components and dE/dx is commonly referred to as the stopping power. Here is it broken up into it's two main components. There exists a third component due to radiation, but for all intensive purposes, this term is neglected. The stopping power is often measured in terms of electron-volts per Angstrom (eV/$\mathring{A}$) and represents the energy loss per distance traversed in the material.

$$\frac{dE}{dx} = -\left.\frac{dE}{dx}\right|_n + \left.\frac{dE}{dx}\right|_e , \tag{2.6}$$

The process of electronic stopping is typically both elastic and inelastic, although the inelastic scattering dominates. This process involves excitation and ionization of electrons over the duration of the ion track. This means that electronic energy losses can be viewed in terms of a continuous slowing down theory. Nuclear stopping is considered to be typically elastic, as it involves large energy transfers through large angular deflections between the projectile and the target as a whole.
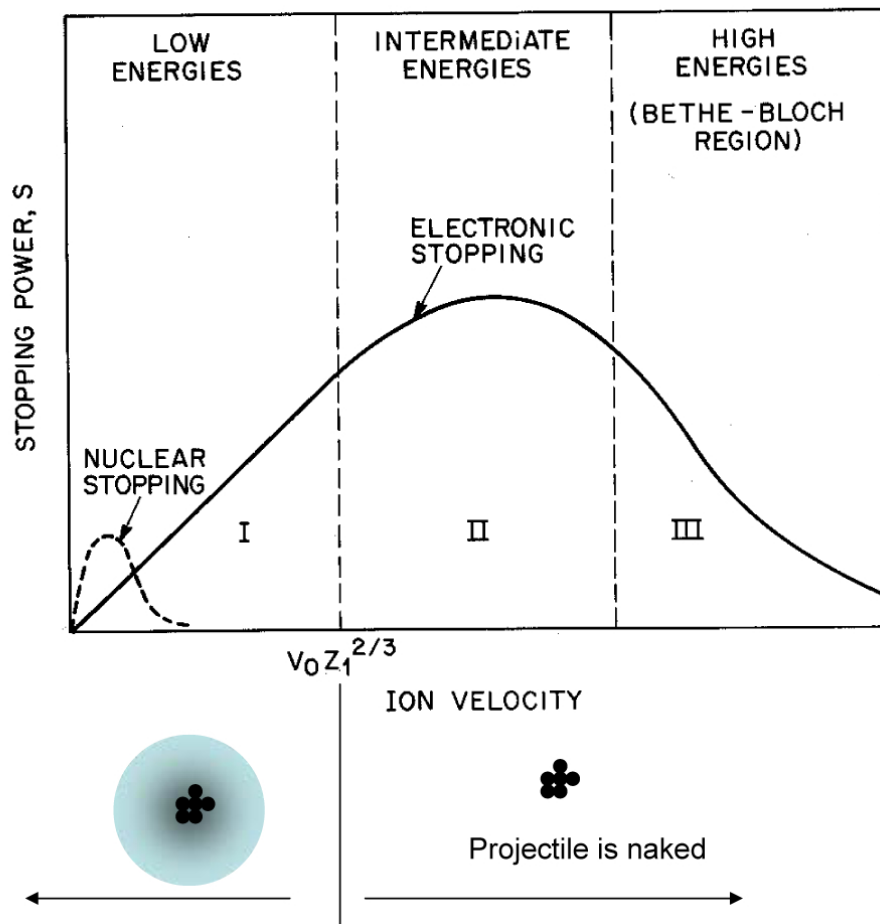
Fig. 4. Illustration of the regimes of dominance for nuclear and electronic stopping as a function of energy. At sufficiently high energies the projectile is considered to be stripped of electrons and fully ionized, whereas in the low energy regime the projectile is considered neutral (naked).

a.   Electronic Stopping

At high ion velocities, energy losses are primarily through inelastic collisions with electrons in the form of electron excitation and ionization. In the limit of very high ion velocity, the ion can be viewed as a moving point charge which is traveling faster than the mean orbital velocities of the target atoms. This limit is known as the Bohr velocity, which is about 2.2×10^6 m/s, or about 1% the speed of light. Bohr himself suggested a correlation to determine the amount of ionization based on velocity and atomic number, the effective ion charge fraction is equal to $v/v_0 Z^{2/3}$, where v and Z are the velocity and atomic number of the projectile. In the limit that the effective ion charge is equal to unity, then the ion is considered to be fully stripped of all it's electrons. In the other limiting case of effective charge equal to 0, the ion is neutral as it is carrying all the electrons with it. The establishes a natural boundary between electronic stopping and nuclear stopping. The approximate velocity that separates the two regimes is given by $v > v_0 Z^{2/3}$ which is the velocity at which the ion becomes fully stripped of electrons. Although this correlation works well for light ions, there is an experimentally validated correlation that applies for heavy ions. This expression is given as $1 - exp\left(-0.92v/\left(v_0 Z^{2/3}\right)\right)$. As an example, the ion species used for implantation used in the present work is Nickel. The energy needed to fully strip the Nickel ion is roughly 2GeV, whereas for light ions, such as Helium, energies as low as 250 keV can be used.

The nature of the purely Coulombic electronic stopping necessarily means that as the ion traverses the medium, energy is transferred to the target electrons with a maximum energy transfer for head on collisions with target electrons. The net energy transferred in such a collision will be highly dependent on the electronic structure. At very high velocities, this method of slowing will be dominant, but collisions with

target electrons is not the mechanism that induces target atom displacement.

As the effective velocity decreases, $v < v_0 Z^{2/3}$, the ion starts to accumulate electrons as the ion is now traveling at velocities less than most of the orbital electron velocity. In this case, the electronic stopping mechanism is not completely understood and several theories prevail.

The model offered by Firsov [30] offers the following explanation. During the collision event, if the ion gains an electron, the momentum is transferred to the electron. This additional momentum accelerates the electron to a given velocity, v which reduces the energy of the incident projectile. His theory suggests that for a short period of time a quasi molecule exists in which case electrons are "shared". An illustration of this process is seen in Figure 5, taken from [28].
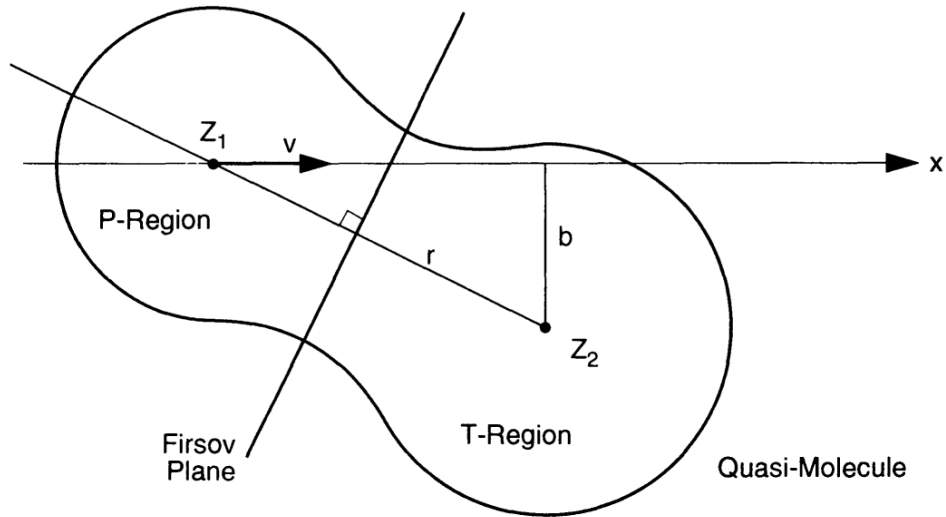
Fig. 5. The Firsov quasi molecule, depicting the P-region, T-region and Firsov plane
formed during electron stopping in the limit of $v < v_0 Z^{2/3}$

The projectile is traveling in the x direction with velocity v and separated in the y direction by a distance b from the central force, as mentioned previously. Firsov suggested that the quasi-molecule consisted of two zones, the P-zone and T-zone for

the projectile and target, respectively. The plane that separates this two zones is termed the Firsov plane. By moving through the Firsov plane the projectile gains electrons from the target, therefore determining the energy needed for this to occur is equivalent to the energy loss by the projectile.

b. Nuclear Stopping

At low ion velocities, the collisions involve the projectile and the target atom as a whole, in comparison to high velocities where individual electrons are involved in the process. This type of collision is by and large elastic in nature and can be described by the typical two body scattering described previously. The energy transfer and deflection angles are large for this type of event as the relative difference in mass of the projectile to the target is much smaller than in the case of electron interactions. As the low energy projectile nears the target atom, the forces experienced by the participants is that provided by the Coulomb interaction and can described by Coulomb potential scattering.

Due to the collision taking place between the projectile and the target atom as a whole and the large energy transfers, this type of interaction can lead to atomic displacements. In order to displace a target atom, a minimum amount of energy must be transferred to the target to dislodge it from its current potential well. The energy necessary to make this happen is called the displacement energy. In typical solids, the solid state configuration represents a local minima of the free energy of the system. Therefore, to to displace an an atom from its current location and become mobile, enough energy must be supplied to overcome this barrier. Should a collision result in an amount of energy transfer that is less than the displacement energy, the collision will not result in the target atom becoming mobile. The energy imparted to the target will be dissipated in the form of lattice vibrations.

On the other hand, if the energy transferred is greater than the displacement energy, the target atom will become mobile and the atom is termed a primary knock-on atom (PKA) and may go on to displace other atoms from their respective sites. This process is the foundation of the damage cascade which is the topic of the following chapter.

CHAPTER III

THE DAMAGE CASCADE

During the nuclear stopping process, projectiles are able to dislodge target atoms from their present location and create a PKA. If the energy transfer is large, the PKA can continue the knock-on-atom process and induce further displacements. This process is commonly referred to as a displacement cascade. The displacement cascade (damage cascade) is thought to progress in a series of stages. The first is the collisional phase, where a PKA initiates a cascade of displacements until such time that its energy is not sufficient to produce subsequent displacements. Next, is the thermal spike phase in which the energy due to the collisions is shared amongst nearest neighbors. After the energy has been dissipated, the material is said to have undergone a quench, or reached thermodynamic equilibrium. The annealing stage is the final stage where defects, created by the damage cascade, find their final location. The first three phases are of particular importance and their description is the subject of the present chapter.

A.   Primary Knock-on Atom Displacements

The model proposed by Kinchin and Pease [31], which employs the hard sphere approximation and the assumption of stationary targets, is often used to calculate the average number of displaced atoms in a sample during ion irradiation. There are of course, more extravagant models such as the Norgett, Robinson and Torrens (NRT) model which accounts for inelastic energy loss using Lindhard's theory, but they will not be discussed herein.

The Kinchin-Pease model assumes a random target and the initial PKA is assumed to have energy T. The displacement energy, E_d, of the target takes a value

which has been averaged over the range of displacement energies. If a target atom receives an energy $T > E_d$, the atom is liberated from its present location and in turn becomes a PKA, whereas if $T < E_d$, the atom remains in the present location. At energies between $E_d < T < 2E_d$, the collision process has only enough energy to liberate one atom before the energy is below the threshold energy of E_d. If nuclear stopping were the only mechanism, this would be the end of the model, where the average number of displacements would simply be incident energy divided by two times the displacement energy, but electronic stopping must also be taken into consideration. For this reason a cutoff value of $T = E_c$ is introduced such that no displacements can take place until the energy is lowered below E_c. For energies lying between $2E_d < T < E_c$, the average number of displacements is just $T/(2E_d)$. A summary of the Kinchin-Pease model is provided.

$$
\text{average number of displacements} =
\begin{cases}
0, & T < E_d \\[1.5ex]
1, & E_d < T < 2E_d \\[1.5ex]
\dfrac{T}{2E_d}, & 2E_d < T < E_c \\[1.5ex]
\dfrac{E_c}{2E_d}, & T \geq E_c
\end{cases}
\tag{3.1}
$$

If the energy deposition as a function of depth, $F_d(x)$ is known or tabulated, an approximation can be used to determine the number of displacements per atom (dpa), from the fluence(ions-cm^{-2}). This relationship is given by,

$$
dpa(x) = \frac{.4F_d(x)}{NE_d}\Phi
\tag{3.2}
$$

where again Φ is the fluence, $F_d(x)$ is the energy distribution function, N is the num-

ber of displacements and E_d is the displacement energy. A graphical representation of this model can be seen in Figure 6.

In the Kinchin-Pease model, there is no real absolute accounting for the spatial distribution during the damage cascade. Understanding the number of displaced atoms is important, but also being able to predict there relative proximity to one another is essential to understand what a damaged region looks like.
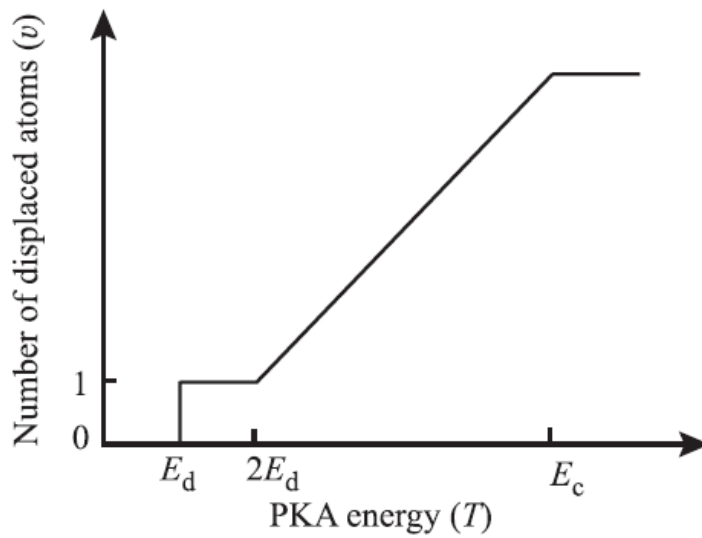
Fig. 6. Graphical depiction of the Kinchin-Pease model.

B. Displacement Mean Free Path

The distribution of damaged regions caused by collisions is determined by the displacement mean free path. The mean free path is defined as the average distance traveled per interaction

$$\lambda = \frac{1}{N\sigma} \tag{3.3}$$

where N is the number density, σ is the cross section. The cross section can be thought of as a likelihood for an interaction and can be derived from quantum mechanics. The relationship between the cross section and the displacement cross section, σ_d can be expressed by,

$$\sigma_d(E) = \int_{E_d}^{E} \sigma(E' \to E)dE'.$$ (3.4)

where E_d is the displacement energy, E is the energy of final energy and E' is the initial energy. This therefore represents the cross section for transferring energies in excess of the displacement energy. Using the hard sphere approximation and the Born-Mayer potential to evaluate σ gives:

$$\sigma_d(E) = \pi B^2 \left[ln\left(\frac{2A}{E}\right) \right]^2 \left(1 - \frac{E_d}{E}\right)$$ (3.5)

where again, the constants A and B are determined experimentally and the mean displacement mean free path, λ_d becomes

$$\lambda_d = \frac{1}{N\pi B^2 \left[ln\left(\frac{2A}{E}\right) \right]^2 \left(1 - \frac{E_d}{E}\right)}.$$ (3.6)

At large recoil atom energies the mean free path is large and therefore the distance between successive collisions is well separated. As the energy of the projectile decreases, the spacing between collisions approaches the order of atomic spacing and at this point each atom along the path is displaced. The damage from this can no longer be thought of as a collection of point defects and it instead leaves behind a highly damaged volume consisting of a shell of interstitials and a core of vacancies [32]. This leads to the notion of a displacement spike. An illustration of the displacement spike which highlights the shell of interstitials and the core of vacancies can be seen in Figure 7, taken from [29].
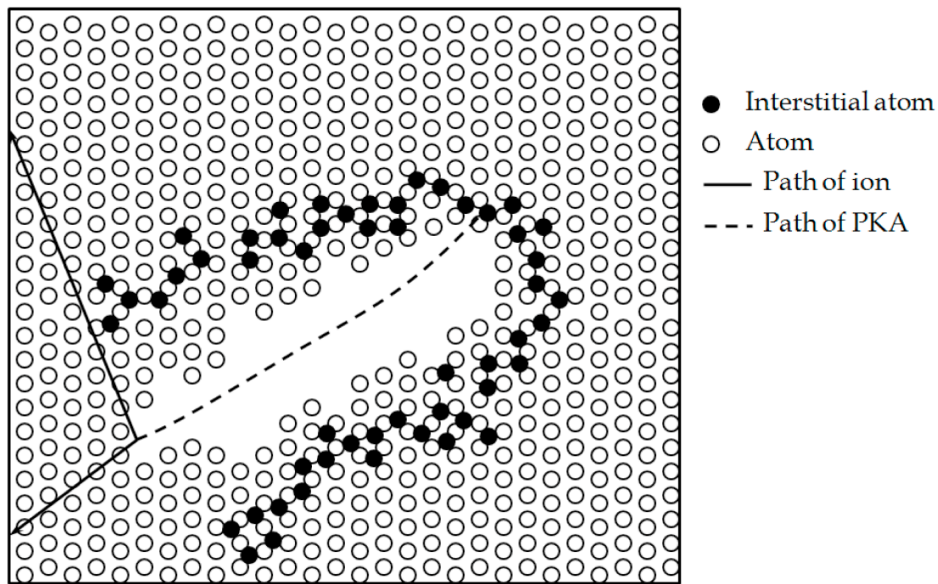
Fig. 7. Illustration of the displacement spike as a result of collisions occurring with a displacement mean free path on the order of the average atomic spacing.

C.   Thermal Spike and Annealing

At the end of the displacement spike, a highly localized region has received a large amount of energy in a very short period of time. In typical two body collisions, the energy transfer can be solved analytically, but in the case of many body collisions, as in the case of a recoil coming to rest, the problem is not so simple. The energy due to the collisions is transferred between many atoms and the result is a net increase in temperature around that region shared amongst nearest neighbors. The heat spike therefore is mainly attributable to nuclear stopping processes since these are mechanisms by which displacements and many body collisions occur. The time scales over which these high temperatures persist are on the order of picoseconds and quickly cool to ambient temperatures. A simple correlation has been suggested [28] to place

a lifetime on the thermal spike induced by a damage cascade, given by

$$t = r^2/4D_t \tag{3.7}$$

where t is the lifetime of the thermal spike, r is the radius over which the energy is deposited and D_t is the thermal diffusivity.

During this time, atoms are able to freely migrate and the resulting number of defects that occur is much less than the initial amount created by the damage cascade [29]. At this time, a thermodynamic equilibrium is established and the quench has considered to have occured. The final annealing occurs due to thermally activated diffusion. This stage lasts until all the available defects that are able to migrate have done so. This implies that the time for this stage to complete is highly dependent on the temperature and irradiation conditions and occurs over a wide range of time scales.

It has been suggested that the heat generation and subsequent temperature evolution can be modeled using the Fourier heat conduction equation [28]. It is therefore the aim of following chapters to be able to model and predict the time evolution of the energy transfer due to the initial damage cascade. A novel multi-scale modeling approach is suggested that is able to couple the energy transfer and the subsequent temperature profiles in metallic glass. A series of experiments are also performed to investigate the role of the damage cascade induced thermal spike in metallic glass.

CHAPTER IV

CHARACTERISTICS OF METALLIC GLASS

Due to the unique structure of metallic glass, a digression is warranted to discuss the fundamental properties. The following chapter will highlight the structure and production of metallic glass. In addition, ideas relating atomic diffusion to the damage cascade are presented, as previous work has shown that the damage cascade may be a result of a free volume enhancement due to ion irradiation.

A.   Structure of Metallic Glass

The atomic arrangement that exists in metallic glass is a random arrangement of atoms, otherwise known as an amorphous structure. Although no long range order exits, there have been several works that indicate that short range order does in fact exist [4, 33, 34]. In typical crystalline alloys a typical periodic structure persists at room temperature, which has minimized the free energy of the system. There exists little to no barrier for crystallization as the diffusivity of the atoms inside is relatively high and the free energy of the system can therefore reach a minimum in the form of periodic arrangement of atoms.

In the case of metallic glass, the system is not in the lowest energy state, but instead has been "locked" into a metastable state that is able to persist at room temperature. The reason that metallic glass does not form a crystal structure at room temperature is a function of the low diffusivity that is designed into the system when selecting the constituents, and the rapid cooling rate that avoids crystallization [35]. The cooling rate that ensures the end state of an amorphous alloy is known as the critical cooling rate. Initially, critical cooling rates to produce metallic glass were very high, on the order of 10,000 K/s, but the ability to produce amorphous alloys

with critical cooling similar to that of oxide glasses has been demonstrated [2].

The idea of a critical cooling rate is most easily explained by considering the initial state of the liquid metallic glass. Initially, the desired alloying proportions are melted to form a molten solution. In the liquid state, atomic arrangement is random. To produce any glass, rapid melt quenching is employed with the desired state being the same random configuration that existed in the liquid state. Rapid cooling is required to limit the diffusional process that would otherwise minimize the free energy of the system and form crystal structures.

As mentioned previously, the first metallic glasses were produced with very high critical cooling rates that were both costly and difficult, therefore there was a desire to produce metallic glass with much lower cooling rates [36]. The work of Inoue [4] showed that in order to form stable metallic glasses, there are empirical rules that should be followed. The rules are often quoted as as Inoue's three empirical rules for stable metallic glasses. These provide direction for the selection of constituent atoms in the desired metallic glass and have driven down critical cooling rates. The first rule is that the mixture should contain no less than three constituents. This is apparent from the first metallic glasses that were produced. These structures, although initially in an amorphous state, over time were shown to form crystal structures. The second rule is based on the atomic size ratios. Previous studies suggested a relationship between the mismatch in atomic ratio and the stability of the metallic glass [37], which is given at above 12% mismatch in atomic size. The final rule is that the constituents should have large negative mixing enthalpies.

B. Production of Metallic Glass

The first room temperature metallic glass was realized by Klement et al. [1] at California Institute of Technology and were cast as thin films. The reason for thin film samples lie purely with the ability to uniformly quench the melt throughout the sample. The nature of the thin film allowed heat to be dissipated uniformly throughout the specimen. As the critical cooling rates increases, so did the size of the samples that were able to be created, so much that metallic glasses are now classified under two categories. One category is "bulk" samples that are able to be cast with a thickness greater than a millimeter, either through injection molding [38] or spark plasma sintering [39, 12]. The final category is "conventional" samples that are usually created as thin films. Due to the fact that the samples used for analysis in subsequent chapters are of the "conventional" type, the emphasis will be placed there accordingly.

The technique used to create the "conventional" metallic glass samples is that of the Pond Melt Spinning Process [40], aptly named after the Johns Hopkins professor who invented the technique. In this process, a liquid nitrogen cooled copper roller is used to rapidly solidify the molten metallic glass, avoid the crystallization temperature and achieving a critical cooling rate. A schematic is shown in Fig. 8, taken from [41].

Initially, high-purity ingots of the desired constituents are melted under an inert atmosphere (usually Argon) and then injected through a nozzle by high pressure onto a continuously spinning block which is kept at low temperature. The rotating block is able to rapidly dissipate the heat through conduction. Samples which have been cast in this fashion are typically on the order of $20 \mu m$ thick [19], a few millimeters in width and are spun off into ribbons.
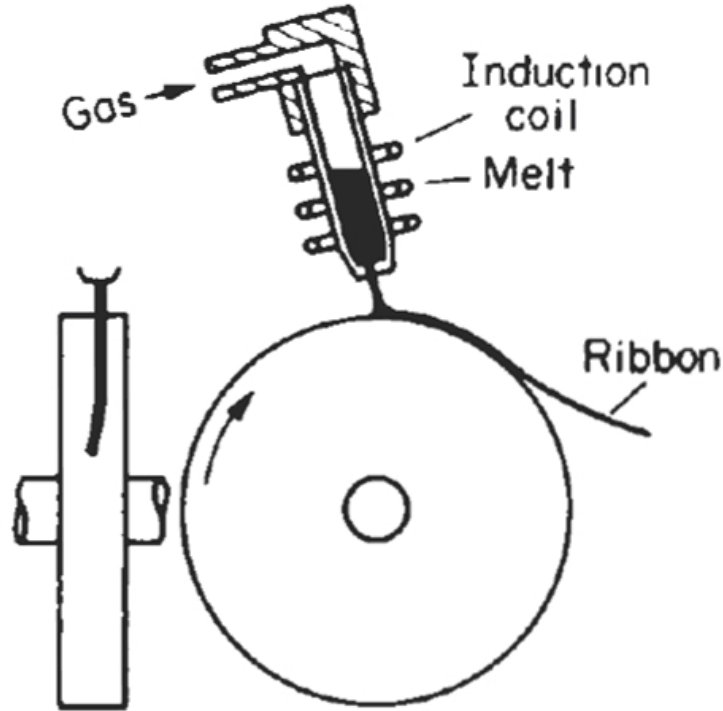
Fig. 8. Schematic of the Pond melt spinning process

C.   Phase Transformations in Metallic Glass

Due to the metastable structure of metallic glass, phase transitions are possible by which the activation energy for crystallization can be overcome. The most obvious method of introducing free energy into the system is through annealing. When the metallic glass is annealed at temperatures above the glass transition temperature and slowly cooled, phase transformations take place [18]. Various other methods have been used to induce small fractions of phase transformations, such as nanoindentation [13], deformation [14], and bending [15]. Ion irradiation induced phase transformations are well documented in general [24], but more specifically with metallic glass there has much interest in the phase transformation process [42, 43, 22]. In addition, Molecular Dynamics [44, 45] has shown that ion irradiation induces free volume changes in

small amounts. The dissertation work by J. Carter [46] has also shown that excess free volume enhances diffusivity and enables nanocrystal formation in metallic glass.

The driving force towards crystallization can be described by a difference in Gibbs free energy between the supercooled liquid and crystalline states. This region is called the supercooled liquid region. The argument presented in the aforementioned dissertation [46] is that either viscosity must change, or the diffusivity must be enhanced in order to achieve crystallization. This conceptual understanding relies on the work of Cohen and Turnbull, which describes the notion of excess free volume in solids.

The free volume model proposed by Cohen and Turnbull [25], adapted for metallic glasses by Spaepen [47], explains atomic mobility in amorphous structures and is used as the model for the diffusivity enhancement. Cohen's theory envisions atomic diffusion based on atomistic jumping from one site to another. In order for an atom to jump, there must be sufficient space to make the jump, else the atom is essentially trapped in its current location. In this way, the diffusion coefficient can be cast in a form based on this probabilistic approach of finding a volume close by to occupy the jumping atom.

The free volume, v_f, can be thought of in terms of the dense packing of spheres. For example, in a cube occupied by spheres, the volume fraction not occupied by the spheres can be considered to be the free volume. The probability that any sphere moves to a new location is a function of how often the sphere attempts the move, and also the likelihood of there existing enough free volume for it to occupy. Spaepen also noted that [47] there exists some activation energy, ΔG, that is needed in order to make a transition for an atom at rest in a potential well. This is incorporated into the theory of Cohen and Turnbull to define a diffusion coefficient that depends on

these parameters, given by

$$D = \frac{1}{6}\nu\lambda^2 exp\left(-\frac{\gamma v^*}{v_f}\right)exp\left(-\frac{\Delta G}{kT}\right) \tag{4.1}$$

where λ is the jump distance, ΔG is the energy required to make the jump, Γ is the jump frequency (approximately given by the Debye frequency), v^* is the volume needed to make the jump, v_f is the total free volume available in the system and γ is a factor that depends on the geometry. The striking quantity of interest is the exponential increase in atomic diffusivity if there is an increase in the free volume of the system. This is argued to play a role in the nanocrystallization of metallic glass.

The argument presented indicates that ion irradiation of metallic glass is able to overcome the activation energy needed to form nanocrystals in small volumes due to the increase in free volume from the damage cascade. An underlying assumption in this work is that the thermal spike induced by the damage cascade is simply too fast for crystal growth and as a result, the nanocrystal formation is due solely to an increase in free volume. For this theory to hold, there should be no observation of direct crystallization inside ion irradiated metallic glass. The reason is simple, if the activation energy for diffusion is overcome in small volumes, it will take a series of steps to ultimately end in a crystal structure. This would be particularly true for metallic glasses that are comprised of many components such as $Ni_{52.5}Nb_{10}Zr_{15}Ti_{15}Pt_{7.5}$ where there is a low diffusivity designed into the system.

In the following chapters the role of the damage cascade and thermal spike will be analyzed. It is critically necessary to build a model that is able to determine if the thermal spike occurs too rapidly to allow for direct crystallization. In addition to this model, experimental verification of this fact needs to be performed to observe the ion irradiated metallic glass to to determine if crystals are observed in regions surrounded by strictly amorphous features or whether it is indeed a collective process

of atomic diffusion.

CHAPTER V

MULTI-SCALE MODELING ION-SOLID INTERACTIONS IN METALLIC GLASS

The overall goal of any multi-scale modeling is to link together phenomena that occur on drastically different time scales. In the present work, the damage cascade creation is thought to progress on the order of femtoseconds [48], whereas the subsequent quenching is on the order of tens of picoseconds [49, 50]. The physics behind the two processes are distinctly different [51], and therefore adequate linking between the two needs to take place using entirely different methods.

This idea is not new, and many attempts, both successful and not, have been made in the realm of multi-scale modeling and physics coupling [49, 52, 53]. A similar approach as the one to be presented has been implemented that involves coupled Monte Carlo (MC) and Finite Element Method (FEM) for use in electron energy transport models [54]. This method, developed at the University of Tennessee, employs the MC approach to calculate the energy and deposition profiles in electron transport, and then performs a coupling to a FEM code that is able to return information pertaining to the temperature profiles. Previous to this, when computational power was quite limited, there was a model developed very similar to the method employed herein that attempts to assess heat transfer from energetic ion irradiation, using the MARLOWE code to model charged particle transport through matter [55]. Since the time of that publication, drastic developments in both code structure and computer architecture has afforded the ability for more accurate modeling, in particular with regard to FEM. Finer meshes, adaptive meshes and parallel computing have enabled the methods we present to couple these two phenomena, and in particular, for the case of metallic glass.

Previous experimental work on ion irradiation in metallic glass has shown that excess free volume likely plays a role in the nanocrystallization of metallic glass, yet without modeling, the significance of the damage cascade may have been overlooked. The motivation for the following multi-scale modeling is therefore quite simple and lies with the following argument. The energy transfer due to a damage cascade is large, and theory postulates the temperatures to be somewhere on the order 10^4 Kelvin, but lasting only a few picoseconds. Therefore, the cooling rate is incredibly high such that the quench occurs so quickly, that although the metallic glass has likely undergone local melting, the minimum critical cooling rate to form glass is present, and therefore the end state is once again amorphous.

It is the goal of the present work to link together the damage cascade formation with the time dependent temperature evolution. In order to achieve this, the MC code SRIM, and a FEM heat transfer code, developed by the author are coupled. A brief background is provided on the theory of the MC approach, as well as that of FEM along with the results of the model.

A. Monte Carlo

The use of MC in this chapter revolves entirely around the ability of the Stopping and Range of Ions in Matter (SRIM) [26] code to be able to predict the damage cascade, in particular for metallic glass. To offer a brief introduction, the SRIM code is a simulation code that runs on the Windows platform and allows the user to predict the effects of ion-solid interactions for virtually any system. Initial code development began around 1985, with later versions being released over the years with the latest revision being that of SRIM 2010.

The operating premise of SRIM is that ion slowing in solids can effectively be

broken into its electronic and nuclear components, as described in previous chapters. Collisions are treated using the BCA and the angle and energy transfer are calculated using the universal screening potential, ZBL potential. The energy required to create displacements is given as a step function, similar to that of the Kinchin-Pease model described previously. There exists no interstitial vacancy recombination and the the targets are treated as amorphous. The ability to quickly evaluate the scattering angle is based on a "magic" formula, using reduced variables introduced by Lindhard, which employs a mean free path such that only large scale deflections in angle are considered [56].

The code is able to calculate stopping powers, ranges, collision locations and energies, for a host of projectile target combinations. Typical input revolves around setting the target stoichiometry, which in the present discussion revolves around $Ni_{52.5}Nb_{10}Zr_{15}Ti_{15}Pt_{7.5}$ metallic glass. The reason that SRIM will be exceedingly useful in the ion irradiation of metallic glass is that the target is amorphous, which is exactly how SRIM handles the calculation.

Figure 9 shows the stopping power of a Ni ion when bombarded into $Ni_{52.5}Nb_{10}Zr_{15}Ti_{15}Pt_{7.5}$ metallic glass. Figure 10 shows the projected range over a host of ion energies in the same material. It can be seen that the approximate projected range of 1 MeV Ni^+ in $Ni_{52.5}Nb_{10}Zr_{15}Ti_{15}Pt_{7.5}$ is ~ 340nm, and the stopping power is equally split in this region between electronic and nuclear stopping. At an initial energy of 1 MeV, the ion will soon begin to slow, and the dominant stopping mechanism soon becomes nuclear stopping.

The output essential for future use in an FEM code is that the contains the details of the collisional process during ion slowing. SRIM is able to output a table of data that includes the location of the scattering event as well as the amount of energy involved in the process. One of the exceptional features of the MC approach
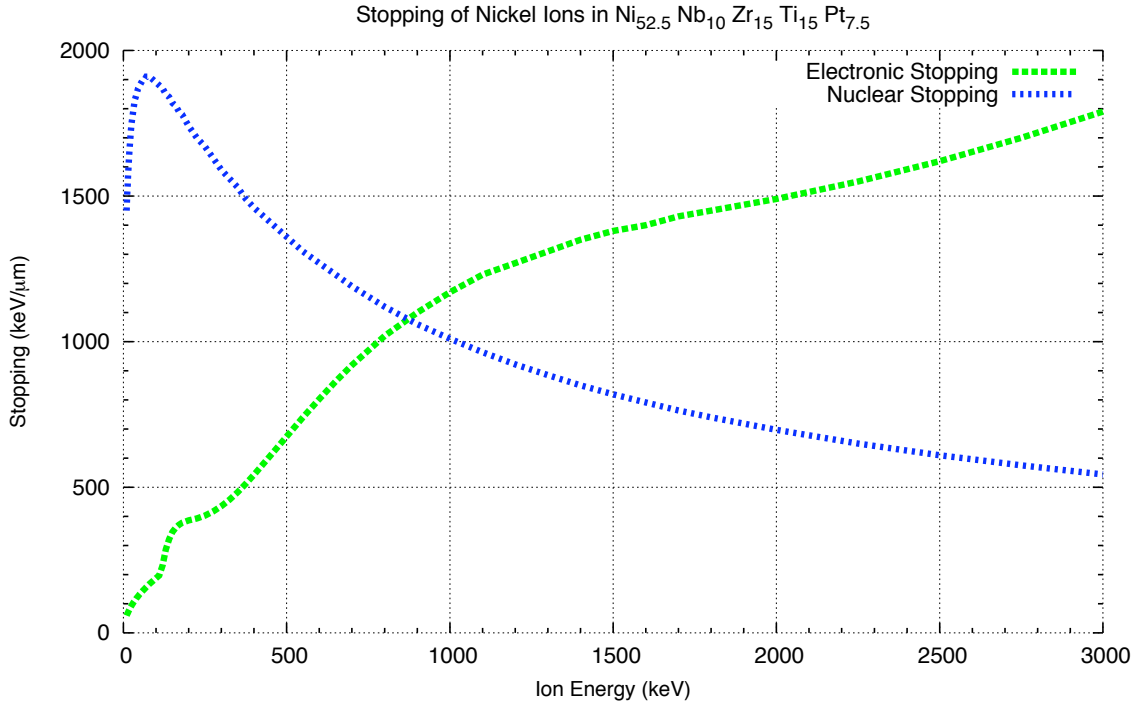
Fig. 9. Stopping predicted due to Ni ion irradiation of $Ni_{52.5}Nb_{10}Zr_{15}Ti_{15}Pt_{7.5}$ by SRIM

is that one can simulate single damage cascades through the use of a random number generator, each being different. Of course, this was not the initial intention of the code, as users would want a statistical average over a large number of MC histories to determine such parameters as Range and Straggling. Nonetheless, the simulation from a single damage cascade in the present discussion is invaluable as it is the basis for calculating energy transfer due to a damage cascade.

For the present study, a single 1 MeV Ni^+ ion is incident on $Ni_{52.5}Nb_{10}Zr_{15}Ti_{15}Pt_{7.5}$ and produces a damage cascade. The results of the damage cascade simulation can be seen in Figure 11. As seen from the figure, the resulting damage cascade is not symmetrical and has a shape that is skewed. This is
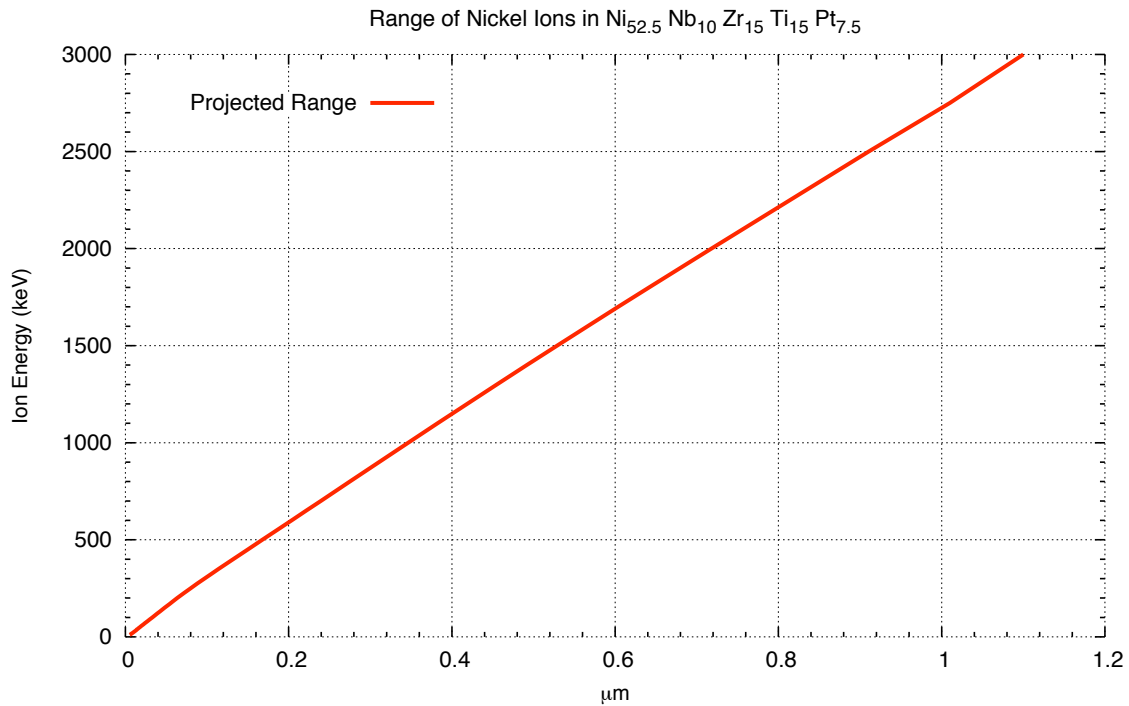
Fig. 10. Range predicted due to Ni ion irradiation of $Ni_{52.5}Nb_{10}Zr_{15}Ti_{15}Pt_{7.5}$ by SRIM

then reflected in the results portion of this chapter when analyzing the shape of the temperature profile.

The output file COLLISON.TXT, as produced by SRIM, contains all the relevant parameters required by the FEM code. To perform the data extraction, a short shell script was written that is able to format the data in such a way that it is readily accessible to the downstream code.

B.   The Finite Element Method

Now that it is understood exactly what will be provided from the MC output, it is now worth devoting a small section to describe the mathematics behind the implementation of FEM.
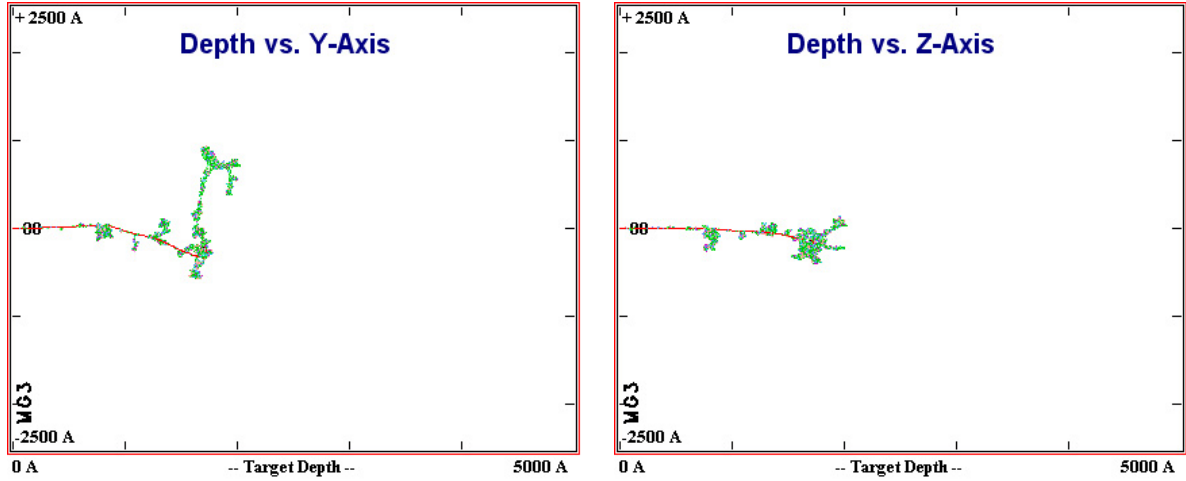
Fig. 11. The spatial distribution of a single damage cascade event induced in $Ni_{52.5}Nb_{10}Zr_{15}Ti_{15}Pt_{7.5}$ due to 1 MeV Ni^+ ion irradiation.

As described above, the source term is what is generated by SRIM, and therefore this serves as input into the FEM code. The locations and kinetic energies of the collisions, due to the damage cascade, are tabulated as output from SRIM. If we consider each collision a point source, the heat transfer equation can be cast in the form,

$$\rho c_p \frac{\partial}{\partial t} T(\vec{r}, t) = \kappa \nabla^2 T(\vec{r}, t) + \sum_{i=1}^{N} Q_i(\vec{r}, t) \tag{5.1}$$

where ρ is material density, c_p is specific heat, $T(\vec{r}, t)$ is the temperature, κ is thermal conductivity and Q_i is a collection of point sources. If in the usual sense, we let

$$\alpha = \frac{\kappa}{\rho c_p} \tag{5.2}$$

then the equation can be written in a familiar form,

$$\frac{\partial}{\partial t} T(\vec{r}, t) = \alpha \nabla^2 T(\vec{r}, t) + \frac{1}{\rho c_p} \sum_{i=1}^{N} Q_i(\vec{r}, t) \tag{5.3}$$

where the problem now lies in solving this second order partial differential equation. The method chosen to solve this problem involves the use of Rothe's method, where

we first discretize this equation in time and solve a series of coupled ordinary differential equations in space. To do this, the Crank-Nicholson time stepping algorithm was employed due to it's ability to handle substantially larger time steps without introducing undue oscillations in the resulting solution. This method is also second order accurate in time, and therefore fits very well with the spatial FEM discretization. Applying the Crank-Nicholson discretization to the time derivative, Equation 5.3 can be written as

$$\frac{T^{n+1} - T^n}{\Delta t} = \frac{1}{2}\left(\alpha\nabla^2 T^{n+1} + \frac{1}{\rho c_p}\sum_{i=1}^{N} Q_i^{n+1} + \alpha\nabla^2 T^n + \frac{1}{\rho c_p}\sum_{i=1}^{N} Q_i^n\right) \qquad (5.4)$$

where the spatial dependence is omitted for clarity. Grouping like terms yields,

$$\left(\frac{1}{\Delta t} - \frac{1}{2}\alpha\nabla^2\right)T^{n+1} = \left(-\frac{1}{\Delta t} + \frac{1}{2}\alpha\nabla^2\right)T^n + \frac{1}{2\rho c_p}\left(\sum_{i=1}^{N} Q_i^{n+1} + \sum_{i=1}^{N} Q_i^n\right). \qquad (5.5)$$

This problem has now been reduced to a series of coupled second order ordinary differential equations. In order to make Equation 5.5 uniquely solvable, we impose Dirichlet boundary conditions. We now seek to cast Equation 5.5 into the weak variational form.[27] Therefore we seek solutions of the form

$$T(\vec{r}) = \sum_{k=1}^{m} b_k(\vec{r})T_k \qquad (5.6)$$

where b_k is a shape function, T_k is a weight and m is the number of nodes in the system, we obtain

$$\left(\frac{1}{\Delta t} - \frac{1}{2}\alpha\nabla^2\right)\sum_{k=1}^{m} b_k T_k^{n+1} = \left(-\frac{1}{\Delta t} + \frac{1}{2}\alpha\nabla^2\right)\sum_{k=1}^{m} b_k T_k^n + \frac{1}{2\rho c_p}\left(\sum_{i=1}^{N} Q_i^{n+1} + \sum_{i=1}^{N} Q_i^n\right). \qquad (5.7)$$

Using the assumptions stated above, everything to the right hand side of this equation is known and we are solving for the coefficients T_k^{n+1}. Galerkin's method is equivalent to minimizing the residual [57] and is achieved by multiplying the entire equation by some linear weight function and integrating over the domain. Galerkin's method chose

the weight function to be the same as the shape function, but this is not a requirement to ensure a minimal residual. Performing this operation and and integrating by parts, the left hand side of the problem takes the form,

$$\int_\Omega \frac{1}{\Delta t} \sum_{k=1}^m b_k T_k^{n+1} b_k d\Omega + \frac{\alpha}{2} \int_\Omega \sum_{k=1}^m \nabla b_k \nabla b_k T_k^{n+1} d\Omega = \tag{5.8}$$

and the right hand side takes the form

$$\int_\Omega \frac{1}{\Delta t} \sum_{k=1}^m b_k T_k^n b_k d\Omega - \frac{\alpha}{2} \int_\Omega \sum_{k=1}^m \nabla b_k \nabla b_k T_k^n d\Omega + \frac{1}{2\rho c_p} \left(\sum_{i=1}^N Q_i^{n+1} + \sum_{i=1}^N Q_i^n \right) b_k \tag{5.9}$$

where the domain is given by Ω and we have successfully reduced the problem to first order by imposing that the solution on the boundary is equal to zero. The problem can now be cast in a matrix form where we iteratively solve for the coefficient matrix T_k^{n+1}. It should be noted that no integral appears in the external source, and this is due to the fact that the point sources act like δ functions, simply picking out the value of the integral at that point, which is precisely equal to the magnitude of the source. Using the "dealii" libraries [27], this is about as far as one needs to go with discretization in order to solve the linear system of equations.

With background on the problem in hand, it is safe to now talk about the implementation of a C++ code to solve the aforementioned problem. A long series of steps must be taken in order to solve any problem using the FEM, and these are discussed in detail in reference [57]. To highlight the main steps, they include defining the unit cell, creating a triangulation, choosing the elements, the quadrature rule and then finally performing a mapping from the unit cells to the actual cell. Once this has been achieved, the linear system can be compiled and solved. The process of mapping the element from the unit cell to the actual cell is accomplished using the Jacobian, the same way that any parameterized curve is handled and the shape functions and shape gradients are evaluated at the nodal points using Gaussian Quadrature. Initial

grid generation is handled through a particular class in the dealii libraries that is able to generate nearly any regular geometric structure, including spheres, cubes, cones, toruses and various other permutations.

For the particular problem at hand, due to the nature of the discontinuities that exist in the source functions, i.e. δ functions, the use of linear shape functions was employed. As one tries to use higher order polynomials and a coarser mesh, the worse the solution becomes. Negativities plague the solution and it quickly becomes apparent that this approach simply will never work. The only solution to this problem is to use a fine mesh and linear elements. This too poses a problem. The computational time associated with globally refining a mesh, in 3-D, that is sufficiently fine enough to deal with huge gradients and discontinuities is daunting. To overcome this hurdle an adaptive mesh refinement was employed using the notion of Kelly Error Estimators. This type of refinement and coarsening is accomplished using the dealii libraries. The premise behind this is quite simple. Anywhere large gradients are found, the mesh should be refined such that the number of points in that region is increased. On the other hand, if the gradients are particularly low, then the option should be presented to coarsen the mesh. This is done by refining the mesh at 30% of the points with the steepest gradients, and coarsening, 3% of the of the points with the shallowest gradients. One last item should be mentioned. The idea of refinement has certain rules associated with hanging nodes, that is a node that no longer is surrounded by a set of vertices that make up the next nearest node. There can only be a difference in refinement levels of one, and therefore in any region where the mesh has been refined twice, the surrounding nodes must be refined at least once. This acts to increase the level of refinement where it is not necessary, but this is difficult to overcome.

The method chosen for refinement involves solving the first time step repeatedly on successively refined meshes until there are no more refinements possible. This

mesh is then carried forth to all other time steps in the problem. Although the best method would be to periodically allow for the mesh to be updated as the physical situation begins to change, the aforementioned method produced agreeable results given the relative ease of implementation. The idea of the mesh following the physics is slightly more involved and could be the topic of future discussion.

Due to the fact that this is a sparse system of equations, i.e. most entries are precisely zero, a symmetric successive over-relaxation method is employed to enable faster convergence. The pre-conditioner value is set to 1.2. The actual convergence control is performed using the conjugate gradient method in an iterative approach. The convergence criteria is set to 1E-12 and there are 5000 iterations per degree of freedom in the system.

There exists some subtleties when handling point sources in FEM. The key is that they cannot lie on a mesh point or node, so extra code must be written to position each point source off the grid. To do this, the point sources were read into the C++ code in the usual manner, but when locating them in 3-D, if they lied on any of the vertices, the were moved a small amount ϵ such that the fundamental physics of the problem remain in tact, yet the point no longer introduced huge jumps in the nodal values.

The code is compiled for execution on a linux based operating system and is designed to run with a minimal number of inputs. The code requires that you select the constants appropriate for the calculation, in this case they are the experimental values of the density, specific heat and thermal conductivity of $Ni_{52.5}Nb_{10}Zr_{15}Ti_{15}Pt_{7.5}$ metallic glass. The user is also required to input the number of time steps involved in the calculation, in the present study this summed to 50 time steps in increments of .5 picoseconds.

Output is handled, again, through the "dealii" libraries. An incredible amount of

work has been placed into parsing meaningful output files through the libraries in vtk and gnuplot formats. The choice of vtk for the present study was obvious due to the nature of the large data sets. Output files for the case under study were on the order of 100MB per time step, with a total of 50 time steps, this sums to approximately 5GB.

The computer code ViSit, developed in part by researchers at Lawrence Livermore National Lab, is used to generate all of the figures in the following section. This interface allows for creating a series of contour plots, volume plots and pseudocolor plots that are invaluable as an analysis tool.

C.   Modeling Assumptions and Results

The previous section described how the coupling occurred between MC and FEM, the particular implentation and the process by which the calculation proceeds. It is the goal of the current section to describe the inherent assumptions in the couple MC/FEM model, but also to discuss the results of the calculation.

The melting temperature of $Ni_{52.5}Nb_{10}Zr_{15}Ti_{15}Pt_{7.5}$ is approximately 950 K, whereas the glass transition temperature is 860 K. This leads to a supercooled liquid region of about 90 K, and this represents the relatively stability against crystallization. The critical cooling rate of $Ni_{52.5}Nb_{10}Zr_{15}Ti_{15}Pt_{7.5}$ is ~ 100K/s [3]. This provides necessary parameters to determine the impact of the damage cascade thermal spike and the subsequent time evolution of the temperature profile. An analysis will be performed with regard to these parameters to deduce whether the damage cascade could in fact lead to direct crystallization in this metallic glass.

The input to the code is relatively simple, in that the user must only specify the number of time steps, the time step interval and material properties. The input values

used in the present analysis involve a time step of .5 picoseconds and a total of 50 time steps were performed, yielding a calculation over 25 picoseconds. The number of collision events directly leads to the number of point sources, in this case, there were approximately 15,500 sources. The material properties have come from literature, where the measured material density, specific heat and thermal conductivity are used for $Ni_{52.5}Nb_{10}Zr_{15}Ti_{15}Pt_{7.5}$ metallic glass.

The damage cascade is assumed to occur over 1 picosecond, and therefore the total energy, in this case 1 MeV must be deposited over this time interval. Using the Crank-Nicholson cell centered approach, the source is left on over 1 picosecond, or two time steps. Because this is a cell centered average approach, the full strength of the source is not on for the total duration, which would lead to an obvious overestimate of the energy deposition. Instead, the usual averaging of the source is applied at each of the two time steps to ensure that a total of 1 MeV is deposited.

An assumption must be made about the volumetric heat generation rate, therefore the energy is assumed to be dissipated over a volume of 10 nm^3. The energy distribution supplied by the MC code is in eV, therefore a conversion is made to Joules, and with the volume assumed and the time of energy transfer known, the power density due to the source is known.

The total area under consideration in the problem is a parallelepiped which is 600 nm x 600 nm at the base and 1 μm tall. The initial condition is that the temperature is uniform everywhere before the source is turned on at exactly 0 K, and the boundary conditions are imposed such the temperature everywhere on the boundary is 0 K. This enables one to analyze the overall temperature increase instead of a relative increase from a given value.

Figure 12 highlights the overall dimensions of the problem as these are omitted to allow a more in depth profile of future temperature contours. The axes are labeled

Fig. 12. A cross sectional 3-D contour plot showing the temperature of the system due to 1 MeV Ni$^+$ ion irradiation in Ni$_{52.5}$Nb$_{10}$Zr$_{15}$Ti$_{15}$Pt$_{7.5}$ after the "source" has been on for .5 picoseconds. The top shows an overview of the orientation. The domain is defined by a parallelepiped which is 600 nm x 600 nm at the base and 1 μm tall, x, y and z directions respectively. The bottom shows angular views of the top region, where the image has been rotated to permit multiple viewing angles.

and carried through all future figures to allow a comparison from one time step to another without losing track of orientation. It should be noted that the incident ion is approaching from the Z direction, and the temperature is asymmetrical due to the fact that the initial damage cascade modeled in the MC simulation had precisely this form. At this point, the source has effectively been on for half the total duration and the maximum temperature is ~ 5000 K. For the simple sake of convenience the minimum temperature under consideration is that of 50 K. This enables temperature contour profiles that are not overloaded with temperature values in the region of least interest. The bottom portion of Figure 12 shows that the region of the damage cascade that has induced temperatures over 50 K is approximately 100 nm in length. Cross sectional slices are take very near the hottest temperatures to reveal the temperature profiles. Three viewing angles were chosen arbitrarily to depict what the temperature profile looks like. The leftmost contour plot in this figure is rotated nearly 90° to show a side view, where the central contour plot is depicted as head on. The rightmost contour plot is rotated back at an intermediate angle to leftmost.

Figure 13 shows a full 3-D contour plot after the source has been on for the full duration of 1 picosecond. This shows that the maximum temperature achieved in the sample, due to the damage cascade is ~ 5300 K. Again, this figure shows the asymmetrical nature of the damage cascade as modeled. The overall shape depicts temperatures that are above 50 K due to the damage cascade. A comment on the minimum solution being a negative value is warranted. As stated previously, a series of mesh refinements and coarsening take place to permit an accurate solution to the time dependent heat transfer, but the solution is solved on the optimum mesh from the first time step for all proceeding time steps. This causes some slight problems near the boundary where the mesh is coarse and there now start to exist temperature gradients as the heat is transferred away from the source and to the boundary. The
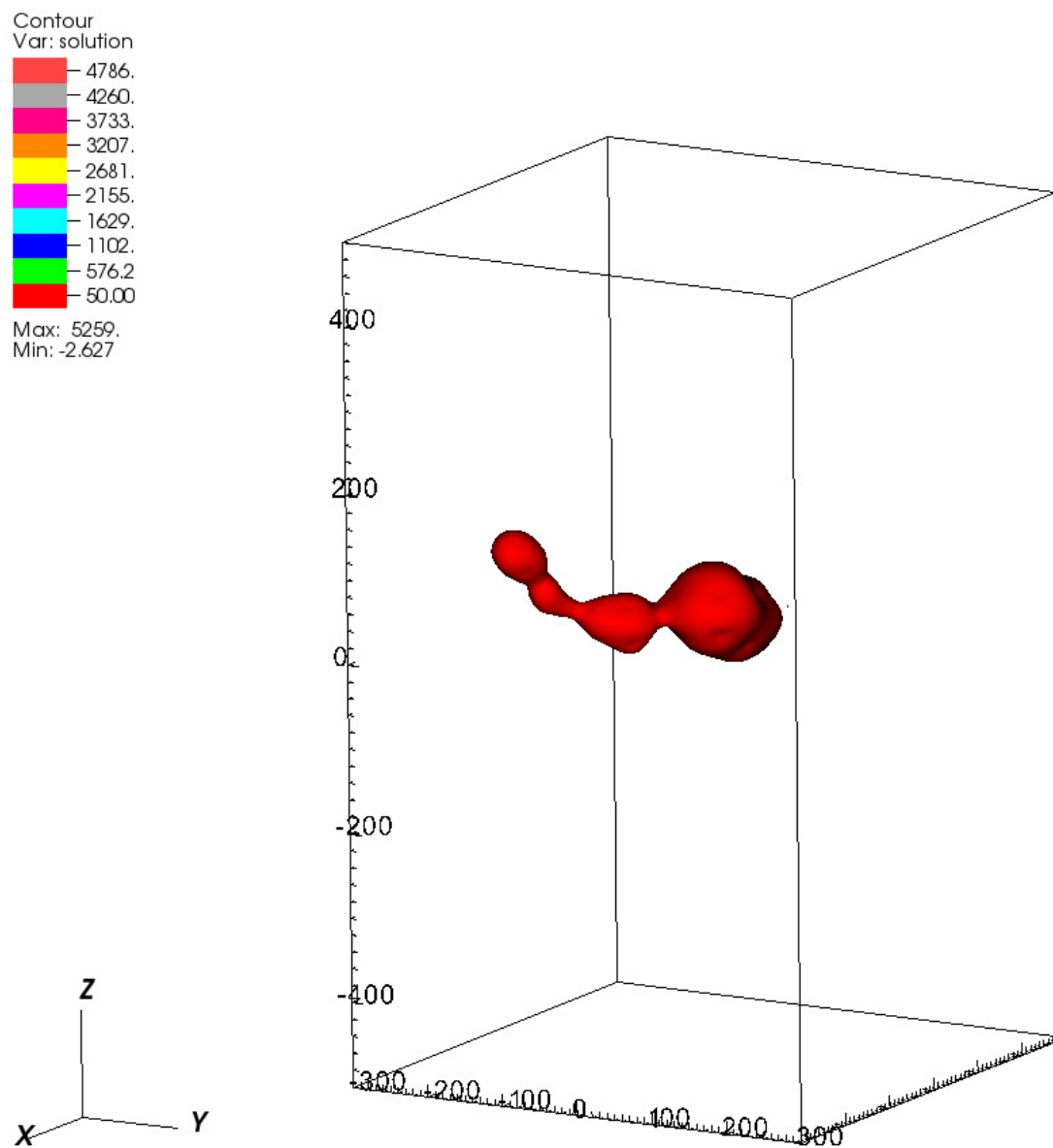
Fig. 13. Full 3-D contour plot highlighting the spatial extent of the damage cascade after the "source" has been on for 1 picosecond.

output files have been analyzed to see where these negativities occur, and indeed they are far from the regions of interest and very near the boundary. One possible method to eliminate these solutions would have been to simply force the solution positive everywhere. A word of caution should be given to this approach. Should one not know that the negativities are far from the region of interest, a violation of conservation of energy might occur without ones knowing as there would be strictly imposed positive solutions that would impact temperature gradients in all future time steps. The author chose to leave the negativities and ensure that they had little bearing on any final result. To offer suggestion for future revisions of the code, the ideal situation would involve that of the physics driving the mesh generation. What is meant by this is that as it stands now, the code generates the finest mesh and carries this mesh forward for all future time steps. What is more desirable is to, at each time step, refine the mesh to follow the physics. At some later time, there would be no longer a need to perform such refinements as the location temperature gradients would be minimal. The implementation of this is not trivial, and therefore in the interest of obtaining results as soon as reasonable achievable, this approach was not taken. This is the exact approach that will be implemented in future revisions.

In order to further investigate the temperature profiles, cross sectional slices will be used in a magnified sense to illustrate the regions of local melting in $Ni_{52.5}Nb_{10}Zr_{15}Ti_{15}Pt_{7.5}$ metallic glass. In Figure 14, the time elapsed is again 1 picosecond and the cross sectional contour plot shows that the regions of peak damage have local melting. There are three distinct regions depicted, each with very high thermal gradients and maximum temperatures in excess of 5000 K. The region to the right, there appears to be local melting in a region consisting of approximately 4 nm, whereas the other two regions of high thermal gradients have melting on the order of 2 nm. The regions between the high density damage areas have relatively smooth

temperature profiles that extend out to the red region, which in this plot is 30 K. The blue regions are those which the temperature is roughly 380 K and the green is about 200 K. Anything inside of the yellow regions are above the melting temperature of $Ni_{52.5}Nb_{10}Zr_{15}Ti_{15}Pt_{7.5}$ metallic glass.
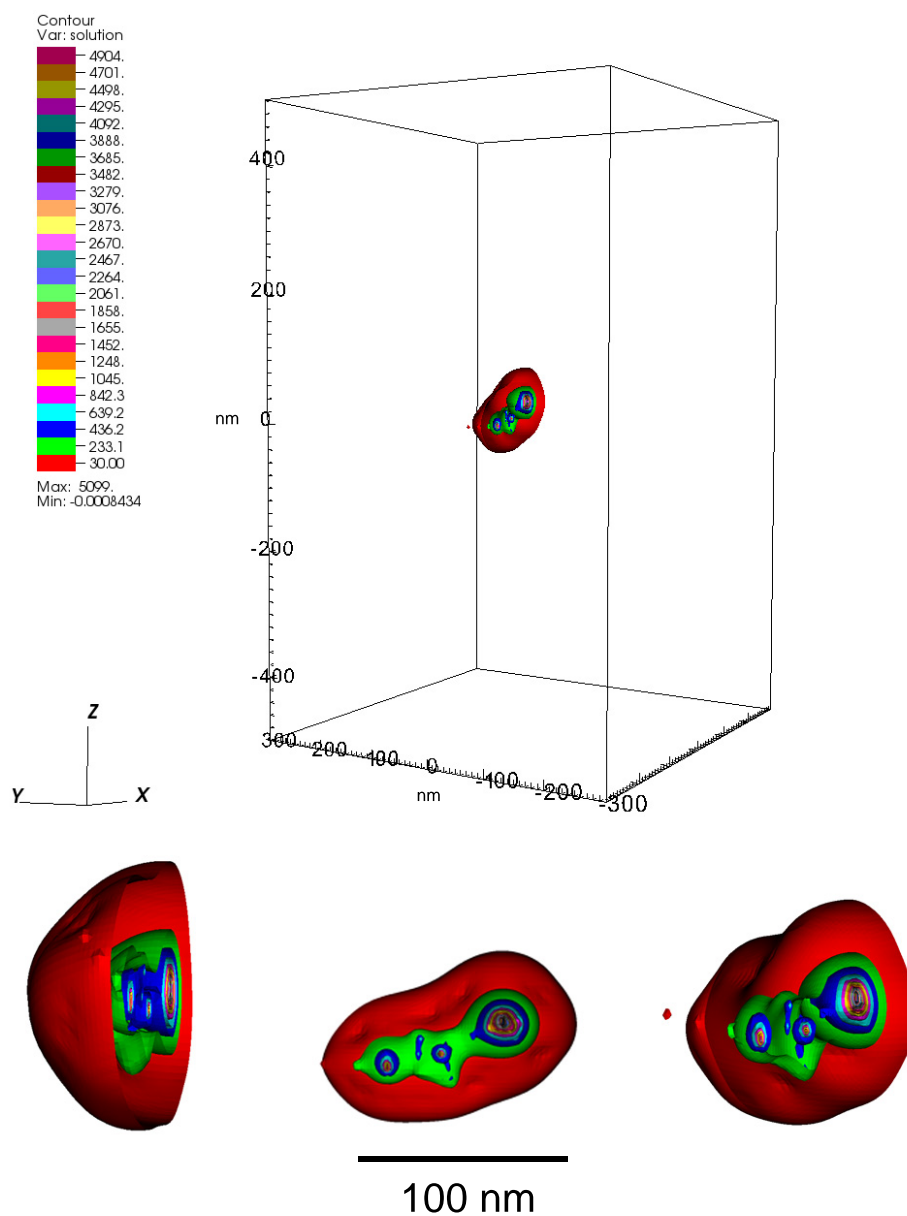

Fig. 14. A cross sectional 3-D contour plot showing the temperature of the system due to 1 MeV Ni^{+} ion irradiation in $Ni_{52.5}Nb_{10}Zr_{15}Ti_{15}Pt_{7.5}$ at the end of the energy transfer from the damage cascade.

Figure 15 depicts a pseudocolor plot of the temperature profile at the end of the damage cascade energy transfer event, or 1 picosecond into the calculation. A cubic slice has been removed for ease in viewing and analysis. The regions which are red/pink are above the melting temperature in $Ni_{52.5}Nb_{10}Zr_{15}Ti_{15}Pt_{7.5}$ metallic glass. This plot is also very useful in visually illustrating what the particular mesh
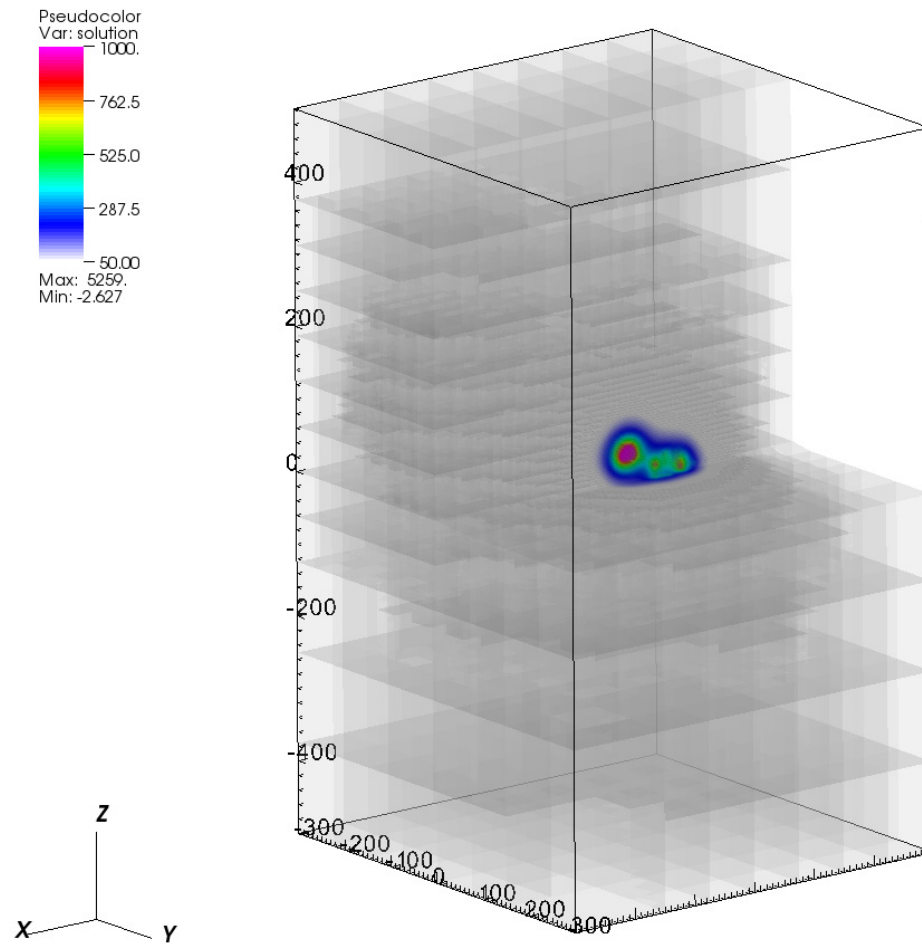
Fig. 15. Pseudocolor plot of the damage cascade, at the end of energy transfer. The mesh is illustrated in this figure. Regions nearer to the source have a finer mesh than those found far from the source. Temperatures in the center of the damage cascade region shown in Pink/Red are above the melting temperature of $Ni_{52.5}Nb_{10}Zr_{15}Ti_{15}Pt_{7.5}$.

carried forth in all time steps looks like. It can be seen that nearest to the peak damage regions, where the source is effectively large, there exists a high number of mesh points. In contrast, far from the source, the mesh is very coarse. This is imperative, as previously stated, because carrying through to each time step a mesh that is simply globally refined is not computationally possible. This would result in an increase in the number of degrees of freedom in the system that would render the problem practically impossible to solve given the current standards in processor power.
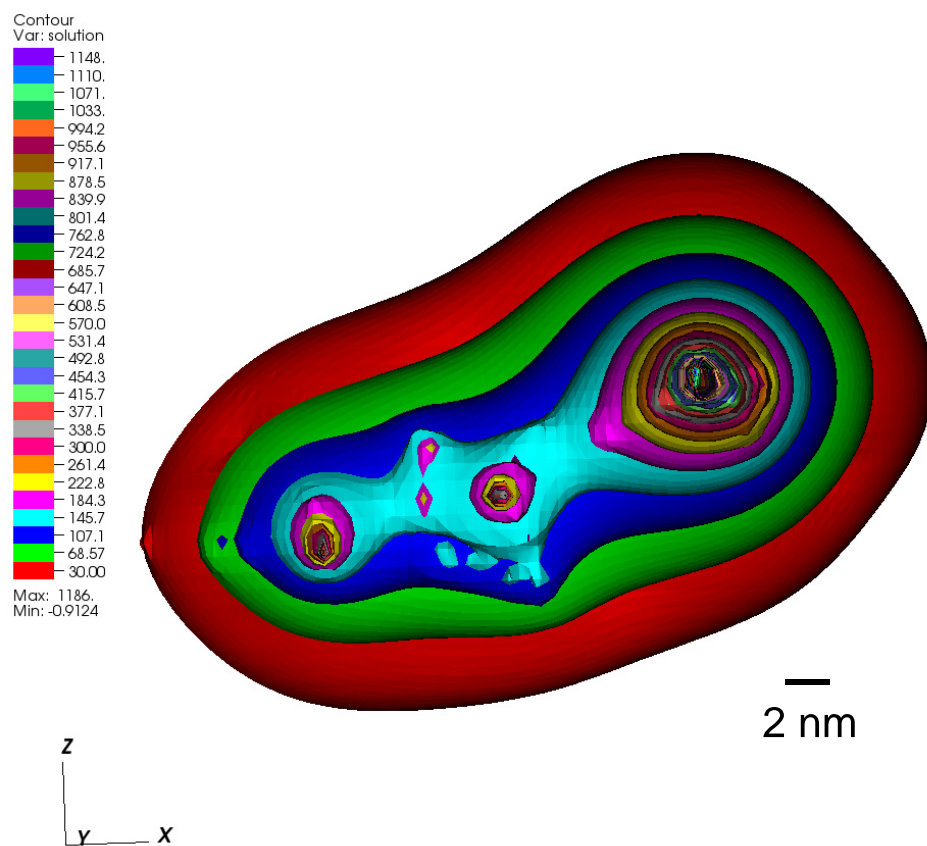
Fig. 16.   A cross sectional 3-D contour plot showing the temperature of the system due to 1 MeV Ni$^+$ ion irradiation in Ni$_{52.5}$Nb$_{10}$Zr$_{15}$Ti$_{15}$Pt$_{7.5}$ after 4 picoseconds have elapsed.

Figure 16 displays a contour plot of what the temperature profile looks like at 4

picoseconds after the damage cascade event. It can be seen that the thermal gradients near the peak damage regions are much lower even after such a short period of time. At this point, the maximum temperature in some regions is still above the melting temperature in $Ni_{52.5}Nb_{10}Zr_{15}Ti_{15}Pt_{7.5}$ although these regions are considerably smaller, less than 1 nm and are difficult to resolve.

Figure 17 displays a contour plot of the temperature profile after 6 picoseconds. The most notable feature of this plot is that the temperature everywhere is below the glass transition temperature. The large thermal gradients that existed in previous time steps are drastically more shallow. Although there are still a large number of temperature contours, the difference between each contour value is much lower than in previous plots. This should be highlighted since this plot and the previous plot seem have similar contours.

The results of the modeling is quite clear. The dynamics of the heat transfer, as a result of the damage cascade, happens very rapidly. The cooling rate can be estimated by knowing the interval between time steps and the relative change in temperature at a given point. Using this method, the cooling rate is estimated to be at 10^{14} K/s $\gg 100$ K/s, which is the critical cooling rate in $Ni_{52.5}Nb_{10}Zr_{15}Ti_{15}Pt_{7.5}$ metallic glass. Given the results, the simulation suggests that it is unlikely that crystallization occurs as a direct result of heat transfer due to the damage cascade. The peak temperature drops below the crystallization temperature in 6 picoseconds and a total time of 20 picoseconds is required to achieve a fairly flat uniform temperature distribution of 50 K in regions where the source existed.
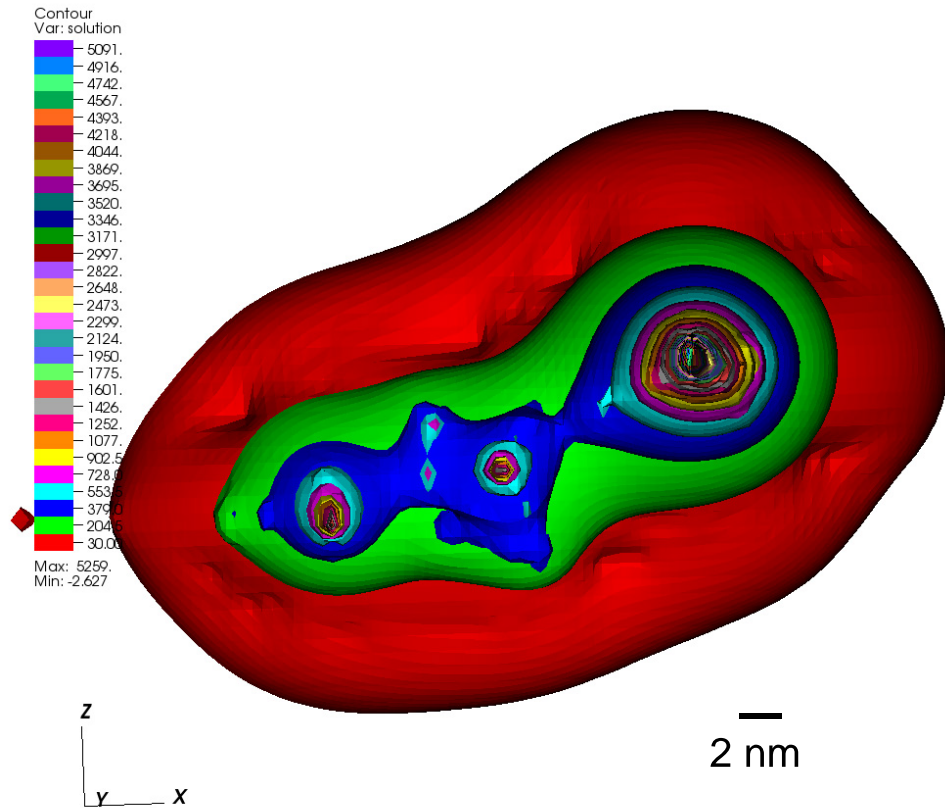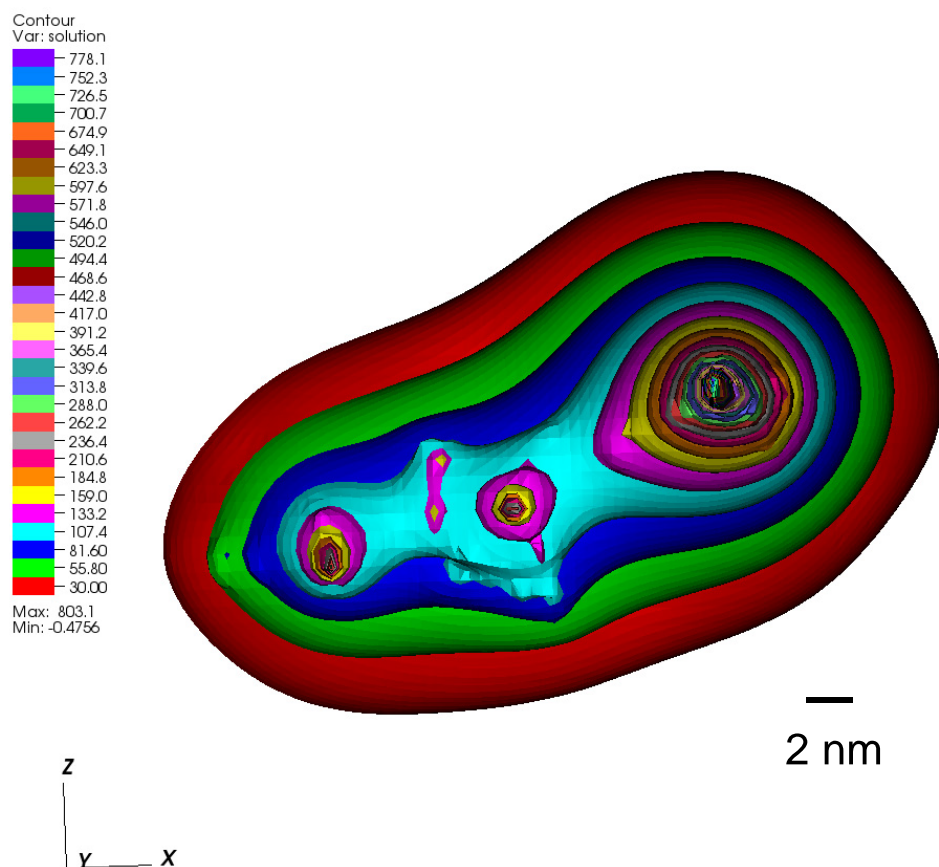
Fig. 17. A cross sectional 3-D contour plot showing the temperature of the system due to 1 MeV Ni$^+$ ion irradiation in Ni$_{52.5}$Nb$_{10}$Zr$_{15}$Ti$_{15}$Pt$_{7.5}$ after 6 picoseconds have elapsed.

CHAPTER VI

EXPERIMENTAL ION-IRRADIATION IN METALLIC GLASS

In order to verify the models that were developed of the damage cascade, and under its role in the nanocrystallization of metallic glass, a series of experiments and material characterizations were performed. This chapter will explain the experimental setup, conditions, methods used for characterization and provide the experimental results.

The amorphous samples of metallic glass were provided through a collaboration with Tohoku University, Japan. The process to create the samples involves a liquid nitrogen cooled copper roller used to rapidly solidify a liquid metal solution of $Ni_{52.5}Nb_{10}Zr_{15}Ti_{15}Pt_{7.5}$, producing a metallic glass sample 20 μm thick and 1.5 mm wide.

A. Irradiation

The 1 MeV Ni$^+$ ion irradiation was performed using an NEC 1.7 MeV tandem accelerator at a beam current of 160 nA cm^{-2} to a fluence of $1\text{x}10^{16}$ cm^{-2} at the University of Houston. Ultra-high vacuum was maintained to eliminate any recombination inside the beam line. In an attempt to systematically study only effects from the damage cascade and to eliminate chemical interactions, self-ion irradiation using Ni ions was chosen, in particular due to the large atomic fraction of Ni in the as-spun specimen. Following irradiation, the samples were prepared for characterization, described in the subsequent sections.

B.   Sample Preparation

There are many ways to prepare electron transparent specimen which can be analyzed using transmission electron microscopy (TEM), but the current work will focus on the conventional method that involves mechanically thinning the sample, followed by ion irradiation in an ion mill. To this end, there are two main types of sample preparation, plane-view and cross sectional. As the names imply, the plane-view sample consists of a sample which has been prepared such that the near surface is the region to interest. No information is obtained over the depth of the sample. The cross-sectional method allows for depth characterization by gluing two pieces of sample together so that their interface is preserved and then the sample is thinned to electron transparency.

The sample thinning procedure will progress differently depending on whether the sample is cross-sectional or plane view. The first description will be of plane view which is the least time consuming, followed by cross-sectional.

1.   Sample Thinning

It should be noted that various problems can arise while preparing specimens of metallic glass [58] due to its metastable state. These include introducing artifacts of the sample preparation, such as ion milling into the end state and mistakenly identifying these as a product of the 1 MeV Ni$^+$ irradiation. Systematic steps were taken to avoid these pitfalls.

In the case of plane view TEM sample preparation of metallic glass, the sample must first be attached to a specimen mount using crystal bond, in this case, a pyrex cylinder. The sample is then thinned using a Gatan Disc Grinder on a wet sanding wheel, but only to the extent that the sample lie flat. Next, the sample, still attached to the cylinder is taken to the Gatan Dimple Grinder. The dimpler is a machine

which is able to create a small, semi-spherical notch in a simple with precision down to +/- 2 microns. A rotating copper wheel, wetted with water and diamond paste is used to reduce the sample thickness to approximately 15 microns. As it stands, the sample has been left rough by the dimpler, therefore a separate attachment for the device, called the polishing wheel, is attached. A finer diamond paste, in concert with the cotton polishing wheel are able to remove any surface imperfections. The sample is then ready for final thinning and polishing using an ion milling machine. The ion mill is a small version of an ion accelerator operated at low energy and current. The ion mill is able to preferentially remove atoms from the sample by striking the sample at glacing angles.

Cross-sectional methods of preparing metallic glass proceed slightly different from that of plane view. First, two pieces of metallic glass are glued, using M-Bond, together with their implanted surfaces touching each other. Next, the samples are glued to two pieces of substrate which are located on the outside of the metallic glass. The samples are placed in a vise and time is allowed for the glue to set up. Next, the samples are placed on a pyrex cylinder, and are thinned to approximately 100 microns using the aforementioned disc grinding technique. Once the sample has reached the desired thickness, the sample must be polished using a series of diamond papers, each successively finer than the previous. This is accomplished using a "tri-pod", or what is essentially a sample holder with a series of three micrometers. This is performed to ensure that the sample is flat, such that all subsequent steps are done properly. Upon completion of polishing, the sample is ready to be unattached from the cylinder, typically using acetone. Once removed, the sample is reattached, this time polished side face down. The sample is then dimpled and polished as previously described, with the overall goal being preferential sample thinning at the interface of the two pieces of metallic glass.

All TEM specimens were prepared as described and final polishing was achieved by room temperature 2 keV Ar ion milling using a Fischione 1010 Ion Polishing System. During ion milling the samples were continuously rotated 360° to ensure homogenous etching.

C. Characterization Methods

Characterization of nanocrystallization in metallic glass is performed using both non-destructive and destructive techniques that allow for the ability to probe the physical, chemical and crystal structures. The techniques in the following discussion are vital to gaining insight into the material properties and behavior under ion irradiation.

1. Xray Diffraction (XRD)

X-ray diffraction is one method for non-destructive analysis that is used to characterize crystal and amorphous structure. Due to the wavelength of x-rays being comparable to the size of atoms, this technique is ideal for probing structural arrangement. The operating premise is that x-rays primarily interact with electrons in atoms and when they collide, elastic and inelastic collisions take place, Thomson and Compton Scattering, respectively. In Thomson scattering, the x-rays only experience a shift in momentum and therefore emerge from the scattering event with their initial energy. The Compton scattering process involves an energy transfer between the x-ray and the electron, and the x-ray emerging from the scattering event will be shifted in frequency (energy). Elastic scattering is the primary mechanism for generating diffraction patterns, whereas inelastic scattering is used to probe electronic band structure.

The periodic arrangement of atoms are discrete and provide planes for the x-

rays to reflect. The peak of the x-ray diffraction pattern allows the determination of atomic positions in a material based on constructive interference. Bragg's Law is used to determine the interatomic spacing based on on the maxima in the resulting x-ray diffraction patterns, given by

$$2\,d\,Sin(\theta)\ =\ n\,\lambda \qquad\qquad (6.1)$$

where d is the interatomic spacing, θ is the angle of incidence, n is the integer order of the diffraction peak and λ is the wavelength of the x-ray [59]. A graphical depiction of Bragg's Law can be seen in Figure 18, and it is clear that any diffraction maxima, the result of constructive interference, must satisfy this relationship.
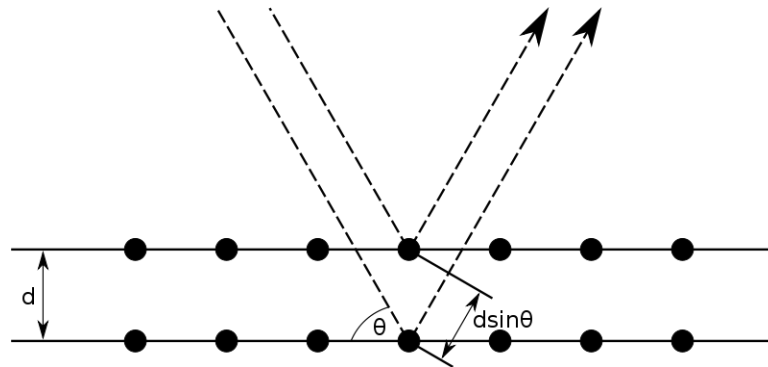
Fig. 18. Illustration of Bragg's Law

A schematic illustration of a typical diffractometer can be seen in Figure 19, taken from [60], where the detector is indicated by D, the source by T and the sample by C. in a typical powder diffractometer, the type used in this experiment, the sample, the detector and the source are all rotated as the desired angular scan is performed.

XRD in this particular experiment was performed using a Bruker-AXS D8 Vario X-ray Powder Diffractometer.
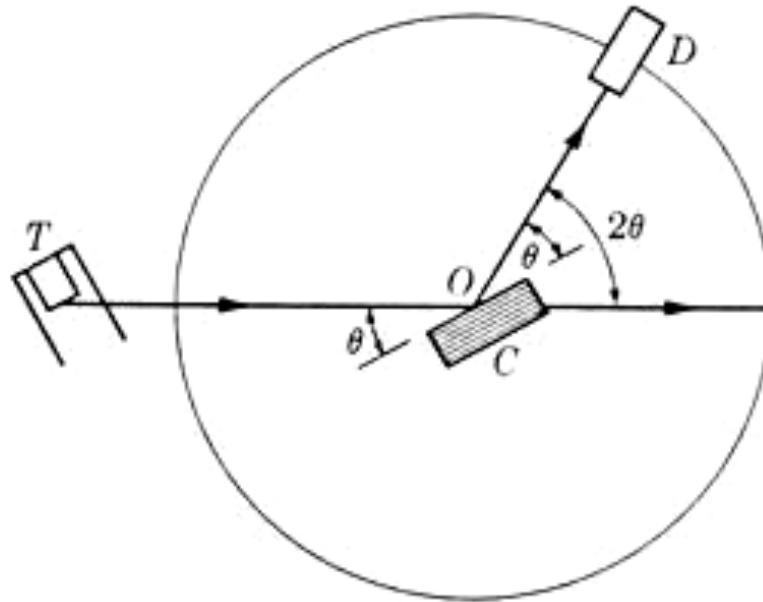
Fig. 19. Diagram of a typical diffractometer setup

2. Transmission Electron Microscopy (TEM)

In a conventional microscope, light is used to image a surface and the resolution is limited by the wavelength of light. In order to overcome this hurdle and resolve images over a thousand times smaller than a light microscope, electrons are used. The small wavelength of an electron enables imaging on an atomic scale. TEM has become the quintessential tool for characterizing and analyzing samples. It is a destructive method whereby samples are first prepared using the aforementioned method, and then analyzed under the microscope. A typical TEM consists of an electron gun, which provides the source, followed by a series of condenser lenses and an objective lens that illuminates an electron beam onto an electron transparent specimen. After passing through the specimen, the transmitted electrons pass through the objective aperture and onto a CCD camera. An illustration of this process is found in Figure 20, taken from [61].
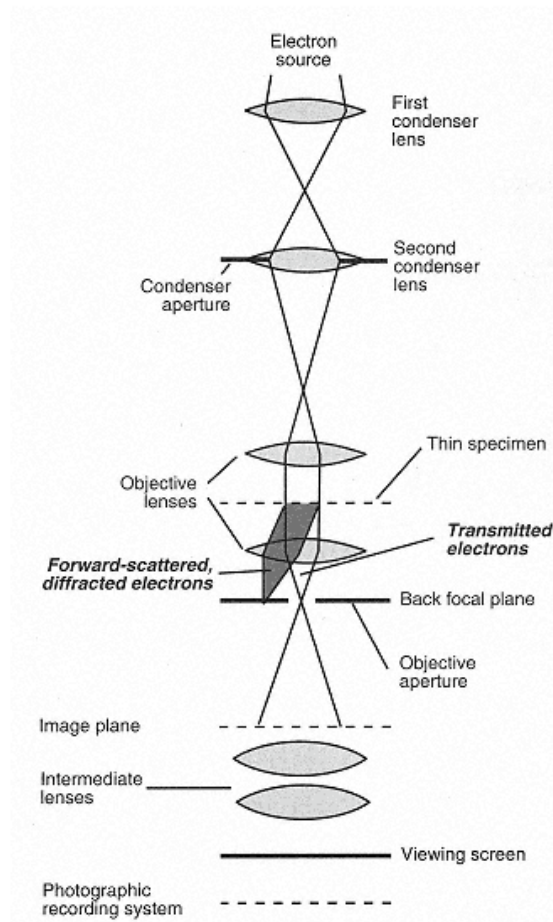
Fig. 20. Illustration of the working principles and components of a transmission electron microscope

Under the category of TEM, there are various methods used to gain insight into the material properties. Bright Field (BF) TEM consists of using a larger fraction of the direct beam to image the specimen, whereas Dark Field (DF) uses the forward scattered, deflected electrons by moving the objective aperture to block the central beam of unscattered electrons. TEM can also be used to create diffraction patterns due to the fact that the diffraction pattern is always present in the back plane of the objective lens. The diffraction pattern can also be imaged and indexed using the

relationship,

$$d = \frac{\lambda L}{R} \tag{6.2}$$

where d represents the lattice spacing, R the distance from the central Bragg peak to the radial peak of intensity (usally a ring, or point), L is the camera length and λ is the electron wavelength. This equation is used in the present study to identify possible crystal orientations that exist in the irradiated metallic glass.

In addition to conventional TEM, Scanning TEM (STEM) employs the same conceptual basis as TEM, except STEM is able to scan a line of interest and determine atomic composition using the principle of Energy Dispersive X-ray Emission (EDX). The same technology can be used in TEM, but the difference is that only a single point in a standard TEM is chosen for analysis, whereas in STEM, there is a line which is scanned. EDX uses the premise that as electrons penetrate the sample, inelastic scattering events will take place that excite target electrons in the material to higher orbits. These excited electrons then de-excite through the emission of characteristic x-rays. The frequency and intensity of these x-rays is then measured to provide insight into composition. A more thorough treatment of the aforementioned topics can be found in Reference [62], including diagrams, operational procedures and a more detailed description of the theoretical basis for electron microscopy.

Transmission electron microscopy (TEM) as well as high-resolution TEM for analysis were performed using a JEOL 2010 microscope operated at 200 keV and equipped with a Gatan SC1000 ORIUS CCD camera. Scanning TEM (STEM) was performed using a FEI Tecnai G2 F20 operated at a terminal voltage of 200 keV, equipped with a Gatan Tridiem GIF-CCD camera and a drift corrected line scan EDS.

D. Experimental Results

XRD analysis was performed on both as-spun $Ni_{52.5}Nb_{10}Zr_{15}Ti_{15}Pt_{7.5}$ sample following room-temperature, 2 keV Ar ion polishing and after 1 MeV Ni^+ ion irradiation. The resulting broad amorphous peak, Figure 21(left) indicates that $Ni_{52.5}Nb_{10}Zr_{15}Ti_{15}Pt_{7.5}$ does not undergo structural transformation during TEM specimen preparation, which has been observed in other amorphous alloys[63]. $Ni_{52.5}Nb_{10}Zr_{15}Ti_{15}Pt_{7.5}$ has a large supercooled liquid region [3] which provides enhanced stability against crystallization under room temperature ion milling. XRD was inconclusive in investigating microstructural changes in the ion irradiated sample, Figure 21(right). The broad, diffuse amorphous peak has been shifted, but no definitive peaks could be identified. The peak to the left in Figure 21(right) is due to the sample holder which has been confirmed by scanning the holder independently.
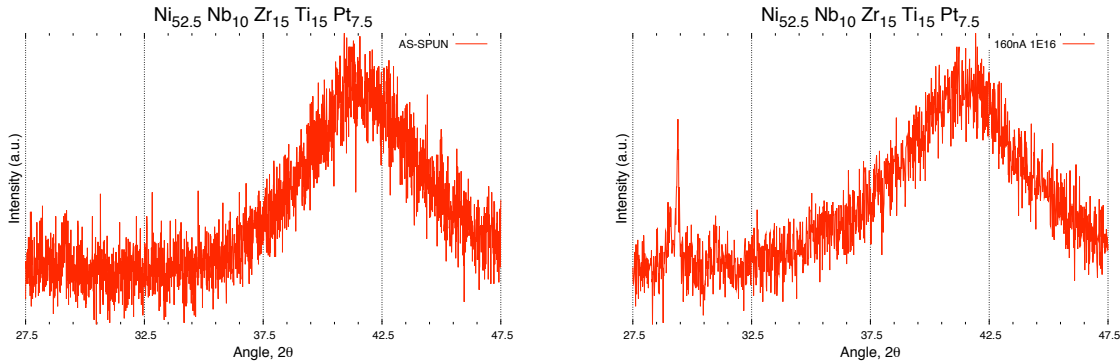
Fig. 21. X-ray diffraction patterns of as as-spun $Ni_{52.5}Nb_{10}Zr_{15}Ti_{15}Pt_{7.5}$ (left) and 1 MeV Ni^+ ion irradiated to a dose of $1x10^{16}$ cm^{-2}(right).

The first set of characterizations focus on plane view samples prepared as previously described. Figure 22(a) shows a bright field TEM micrograph with the corresponding selected area electron diffraction pattern (SAD) from the as-spun $Ni_{52.5}Nb_{10}Zr_{15}Ti_{15}Pt_{7.5}$ ribbon. The featureless bright field TEM micrograph shows

uniform contrast, indicative of an amorphous state, which is further corroborated by the SAD pattern's bright diffuse rings.

Figure 22(b) and 22(c) show bright field and dark field TEM micrographs of $Ni_{52.5}Nb_{10}Zr_{15}Ti_{15}Pt_{7.5}$ subjected to 1 MeV Ni^+ ion irradiation under beam current density of 160 nA cm^{-2} to a fluence of $1x10^{16}$ cm^{-2}. The insets are their respective SAD patterns. The bright field TEM micrograph displays three distinct types of feature (1-3), each of which appear in numerous places throughout the micrograph. Each occurrence of a particular feature is unique, however, similar origin and physical property permits a general discussion of each type of feature. An individual feature from each of the three regions was chosen as typical representative for discussion.

The type of feature labeled as 1 in Figure 22(b) is the amorphous matrix, consisting of concentrations of alloying elements near that of the as-spun proportions. This region is devoid of features and contrast, similar to that of the as-spun TEM micrograph in Figure 22(a). Dispersed within the amorphous matrix is feature 2; a precipitate region consisting of an area of different concentration than that of the as-spun sample. Within this region are varying levels of contrast, owing to a heterogeneous composition, but not necessarily indicating any conclusive degree of crystallinity. Feature 3 is found superimposed on the precipitate region (feature 2), and displays large contrast gradients and a periodic nature, indicative of crystal structure. The inset SAD pattern in Figure 22(b) also indicates the formation of crystal phases.

The dark field TEM micrograph in Figure 22(c) displays a high contrast region which likely to be crystalized, labeled 3', which corresponds to the bright field TEM micrograph location labeled 3. This correlation between the bright and dark field TEM micrographs suggests that the repeating areas of high and low density within the precipitate phase, as seen in the dark field TEM micrograph, are sites for nucleation and growth of crystal phases. A lack of high density regions outside of any of
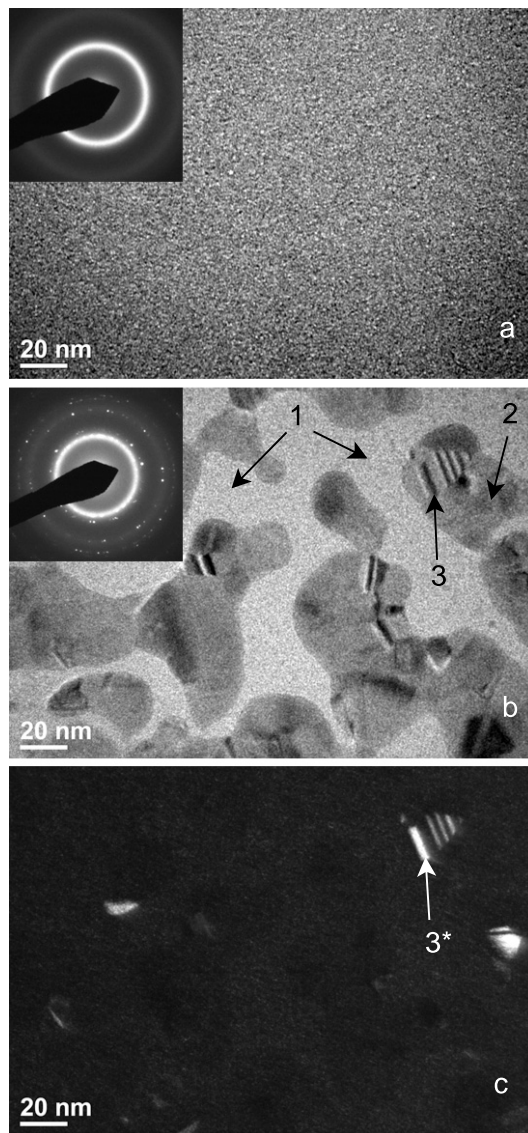
Fig. 22. TEM micrographs with the SAD patterns shown in the inset of (a) as spun $Ni_{52.5}Nb_{10}Zr_{15}Ti_{15}Pt_{7.5}$ after room temperature ion milling at 2 keV, (b) 1 MeV Ni^+ ion irradiated to a dose of $1x10^{16}$ cm^{-2}(c) and the corresponding dark-field micrograph of the same region.

the precipitate islands in the dark field TEM micrograph lends toward a two stage, indirect process for crystal formation and growth as a result of ion irradiation.

The preceding chapter's model has indicated that the energy transfer throughout the metallic glass as a result of the damage cascade happens so quickly that the minimum critical cooling rate is achieved. The aforementioned figures indicate a confirmation of the model developed in the preceding chapter. If nanocrystals were located outside of the precipitate region, it would be reasonable to believe that the damage cascade directly resulted in the formation of crystal structures, but this is not what is observed.

In an effort to better understand the mechanism at work driving the formation of the precipitate and crystal formations, STEM was employed. Figure 23(a) shows a STEM micrograph of the irradiated sample. The same observations previously reported in Figure 22(b) are again observed, but due to the nature of STEM, the regions of high density are the lighter areas, whereas the low density amorphous matrix is a darker color (similar to dark field TEM). The region which has been indicated by a white box is the area which has been chosen for further analysis using energy dispersive x-ray spectroscopy (EDS).

Figure 23(b) is an optically zoomed in micrograph of the region of interest, depicted by a white box in Figure 23(a). The white line found running horizontally through the micrograph is the 100 nm line which was scanned using EDS for atomic composition. Along this 100 nm line are the following regions; the amorphous matrix (leftmost), the precipitate region, an intermediate region segregated from the rest of the amorphous matrix, a crystalline region, and finally another amorphous region. This line was chosen due to the incorporation of all elements previously observed under TEM. The line scan was performed to compare the atomic concentrations in the various regions and to compare the concentrations found in the crystal region
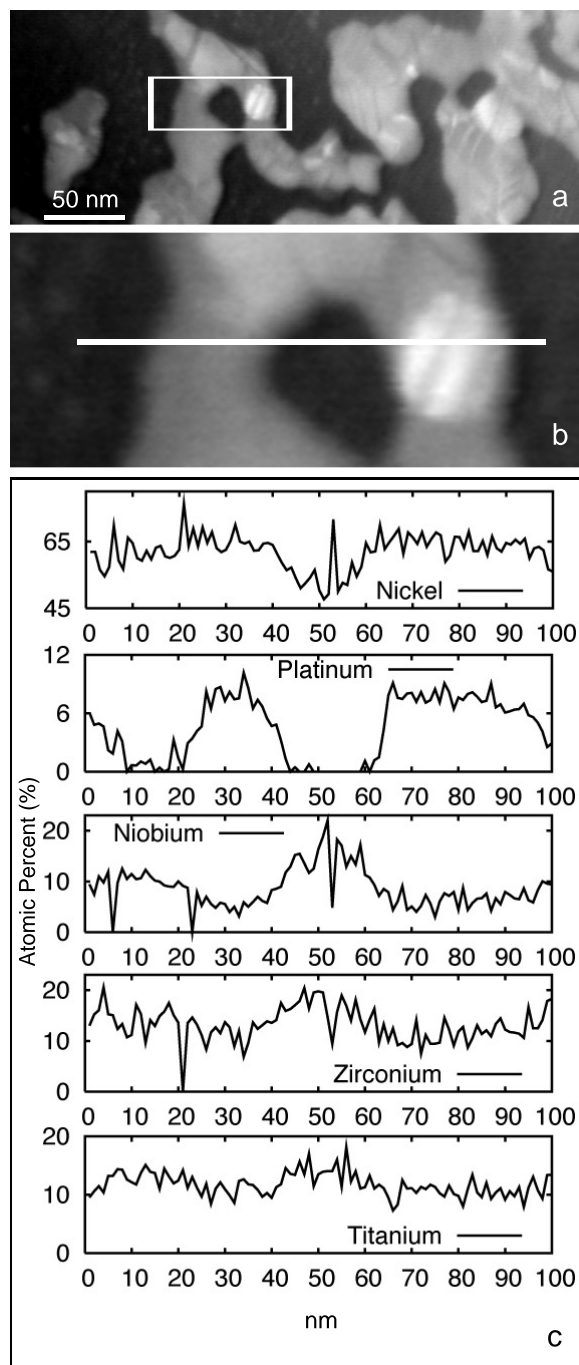
Fig. 23. (a) Scanning TEM micrograph of $Ni_{52.5}Nb_{10}Zr_{15}Ti_{15}Pt_{7.5}$ after 1 MeV Ni^+ ion irradiation with the highlighted area depicting the region an EDS line scan was performed. (b) A magnified view of the 100 nm line which was scanned using EDS and (c) the corresponding plots of concentration along the EDX linescan.

to that of the precipitate region. The characteristic x-rays emitted during electron irradiation were obtained in 1 nm increments for the along the length of the line. The relative intensities were mass corrected to produce a position dependent concentration profile seen in Figure 23(c).

Table I. Calculated d-spacings extracted from SAD of $Ni_{52.5}Nb_{10}Zr_{15}Ti_{15}Pt_{7.5}$ after 1 MeV Ni^+ ion irradiation to a dose of $1x10^{16}$ cm^{-2}. Shown for comparison are standard d-spacings for Ni_3Nb, Ni_3Zr and Ni_3Ti phases. Values are in angstroms $\AA$.

Experimental data	Ni_3Nb Orthorhombic	Ni_3Zr Hexagonal	Ni_3Ti Hexagonal
2.1903	2.21	2.1603	2.2066
1.9040	1.93		1.9485
1.8743			1.8785
1.3328	1.27	1.3317	1.3269
1.1376	1.16	1.1337	
1.0819	1.07	1.08	1.0937
0.8702	0.84	0.8546	
0.7683	0.76	0.7884	
0.06387			

STEM has been able to reveal interesting phenomena from each of the regions and provide possible explanations as to crystal phase, orientation and atomic segregation as a result of ion irradiation. Figure 23(c) indicates a complete segregation of Pt from the central region towards the precipitate phase as well as the crystal. One possible explanation for this due to the negative heat of mixing of Pt with Zr, Ti and Nb at

-100 KJ/mol, -74 KJ/mol and -67 KJ/mol respectively. This fact alone is not enough to explain the phenomena, therefore possible crystal phases were identified using the SAD patterns, binary phase diagrams and known d-spacings from the ICDD database [64]. Table I contains the fitting of the measured diffraction patterns to standard values and indicates the possible phases as Ni_3Nb, Ni_3Ti and Ni_3Zr. The measurement of the d-spacings was performed using Gatan Digital Micrograph and entails the use of Equation 6.2. To ensure the TEM calibration is correct, a known sample of Si is imaged and indexed for comparison at the same time that the diffraction pattern micrographs are aquired. This produces a scaling factor that can be used as a best estimate fitting coefficient.

Table II. Comparison of various parameters involved in the likely substitutional solid solution of $(Ni,Pt)_3Nb$ and $(Ni,Pt)_3Ti$

Element	Atomic Radius (pm)	Electronegativity (Pauling)	Valency	Crystal Structure
Pt	139	2.28	1	fcc
Ni	124	1.91	1	fcc
Nb	146	1.6	1	cubic bc
Ti	147	1.54	2	hexagonal
Zr	160	1.33	2	hcp

The measurement of the crystal phases has uncovered an unlikelihood of Pt crystal phases present, which seems to contradict the apparent high concentrations of Pt in the crystal regions. The underlying mechanism may be the formation of a substitutional solid solution. Table II contains a listing of the relevant parameters involved in the formation of a substitutional solid solution. It can be seen that both Ni and

Pt are both group VIII elements that possess the same electron valency, the same crystal structure (fcc), similar atomic radii and electronegativity. This observation corresponds with the Hume-Rothery rules for forming solid solution. Therefore, it is postulated that Pt is substituting for Ni to form $(Ni,Pt)_3Nb$ and $(Ni,Pt)_3Ti$ and it is the combination of highly negative mixing enthalpies and the ability to readily substitute into a solid solution that the concentration is enhanced in the precipitate and crystal regions. It should be noted that the phases identified under ion irradiation are different from those described under annealing conditions for $Ni_{52.5}Nb_{10}Zr_{15}Ti_{15}Pt_{7.5}$ which had be reported Ni_4Ti [3, 39].

To highlight the features of interest and obtain SAD patterns for a single crystal, HRTEM was performed. Figure 24(a) and 24(b) show SAD patterns from their respective regions marked by arrows in the HRTEM micrograph seen in Figure 24(c). Figure 24(a) has bright diffuse rings, similar to the as spun sample, indicating that this region is completely amorphous. This agrees with the HRTEM micrograph which displays a featureless region with uniform contrast. Figure 24(b) indicates that the region is is most likely crystalline, with a crystal 10nm in size. This again agrees with the HRTEM micrograph which displays a region of high contrast and features characteristic of crystal phases.

In addition to plane view TEM, efforts were made to achieve cross sectional TEM samples. The results of which have been slow coming. One of the apparent draw backs of plane view TEM is the total lack of depth profile and the features present are limited to those of the near surface region. Plane view TEM has been able to reveal a wealth of knowledge on the crystal formation, all but rule out the thermal spike in the crystallization process, but has stopped short of explaining how the damage cascade impacts the material through the depth.

In an attempt to understand the damage cascade as a function of depth in metal-
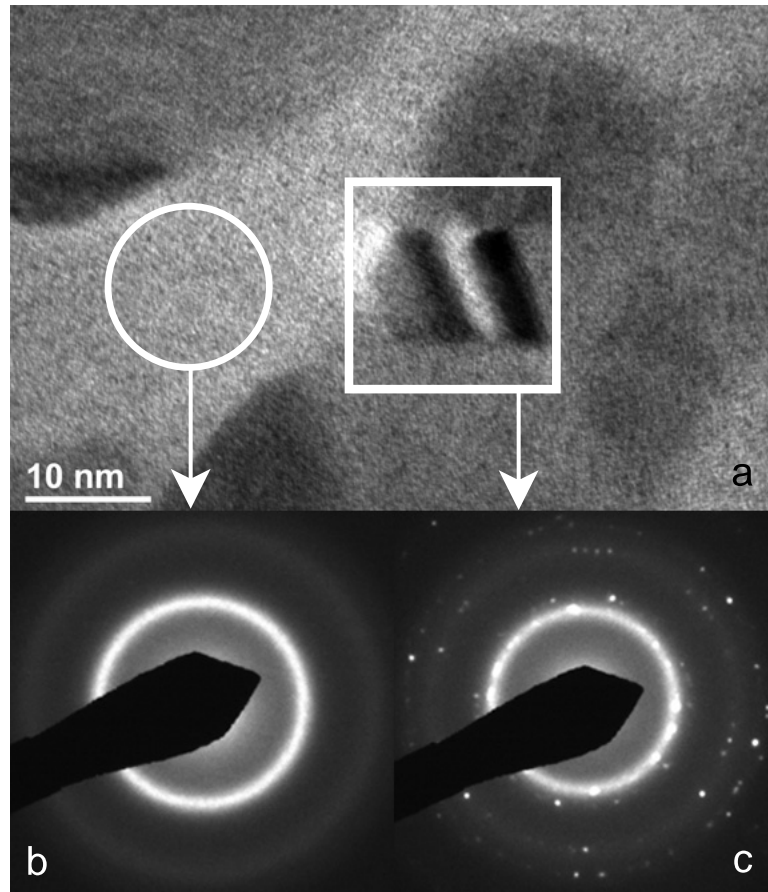
Fig. 24. (a) Bright field HRTEM micrograph highlighting the crystal (square) and amorphous (circle) regions. The corresponding SAD diffraction pattern of the amorphous region (b), and the crystal region (c), respectively.

lic glass a cross sectional approach must be taken. It is this reason that so much time and effort has been placed in this area. It is an understatement to say that producing cross sectional samples has been a great challenge. The reason for this is that the projected range of 1 MeV Ni$^+$ in $Ni_{52.5}Nb_{10}Zr_{15}Ti_{15}Pt_{7.5}$ is roughly 340 nm. Therefore at least double this distance must be preserved to truly obtain accurate information about the damage cascade over the projected range and beyond as well as the surface remaining intact after ion milling. The samples, as previously stated, start out at $20\mu m$ and must be attached to a substrate to even begin to work with them. Finding

a suitable substrate that will dimple and ion mill at the same rate has been a trial and error process.

The best approach uncovered by the author involves the use of SiO_2 as a substrate. Although the metallic glass and the SiO_2 have drastically different ion milling rates, it has been found to be the easiest to work with. Other substrates such as Al_2O_3 and MgO have been tried without much success. Although they seem to ion mill at a more consistent rate, they are difficult to polish and dimple and more often than not result in sample damage and breakage. It is this reason that the work has progressed with strictly using SiO_2.

Another difficulty that arises when preparing cross sectional metallic glass samples is due to that fact that M-Bond does not adhere nearly as well to metallic samples as it does to oxides and various other materials. Frequently, during the process, the sample will separate, rendering the sample unable to be thinned using ion milling. This is due to the fact that if the sample separates, the interface will not be preserved under ion milling as there is no longer a region to shield the interface. The result will be a degradation of the entire sample surface.

With all this in mind, the work does stop short of completely uncovering all the details in the damage cascade depth profile in metallic glass, but it is worth mentioning. Figure 25(a) is a BF XTEM image of the near surface region. What is apparent from this micrograph is that there has been some preferential etching due to ion milling that has either reduced or eliminated a portion of the interface. A SAD pattern from this region reveals that it is highly probably to contain some crystal phases. These diffraction patters appear very similar to those obtained from plane view samples. In addition, similar to plane view TEM, crystal features are observed that appear to only exist in the the grey precipitate regions. This fact is corroborated by the DF TEM image found in Figure 25(b).
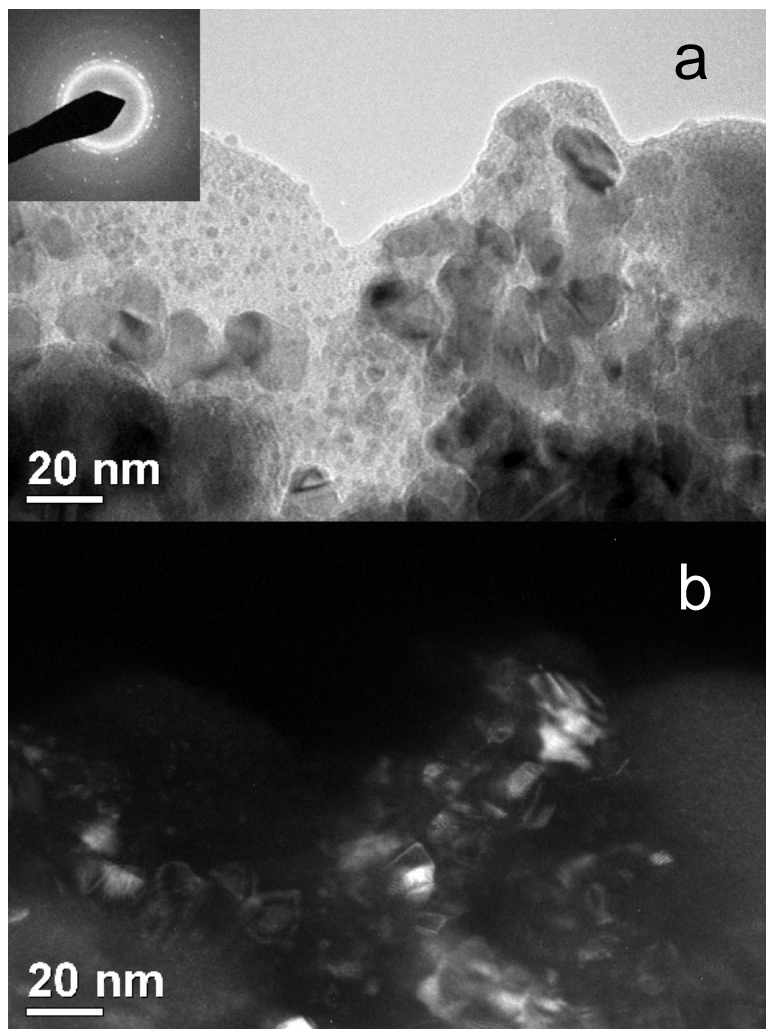
Fig. 25. Cross Sectional TEM micrographs with the SAD patterns shown in the inset of (a) $Ni_{52.5}Nb_{10}Zr_{15}Ti_{15}Pt_{7.5}$ after 1 MeV Ni^+ ion irradiation to a dose of $1x10^{16}$ cm^{-2}(b) and the corresponding dark-field micrograph of the same region.

HRTEM was also performed on this region as seen in Figure 26. The micrograph reveals a nanocrystal, similar in size to that obtained under plane view HRTEM, which is approximately 10 nm in length and 2 nm in width. A series of grey precipitate regions are seen which seem to indicate that this region has been substantially altered from the as-spun amorphous state. Again, HRTEM also shows that the crystal formation is within a grey precipitate phase, leading to another piece of evidence to suggest a two stage crystallization mechanism in this metallic glass.

The experimental results, while not entirely conclusive, do suggest a high likelihood that the crystal formation in $Ni_{52.5}Nb_{10}Zr_{15}Ti_{15}Pt_{7.5}$ metallic glass is not a direct result of the damage cascade. The previous chapter's results suggest that the thermal spike and subsequent heat transfer occur on a scale of 10^{14} K/s, meaning that the cooling rate is much too high for directly form nanocrystals. In the experimental portion of the present study, no crystals are observed outside of the grey precipitate region. This strongly suggests that the crystal formation occurs as a sequence of steps, whereby the metallic glass must first form an intermediate atomic concentration before crystallization can occur. The crystal phases induced by 1 MeV Ni^+ ion irradiation in $Ni_{52.5}Nb_{10}Zr_{15}Ti_{15}Pt_{7.5}$ have been identified along with a theory as to how those phases form.
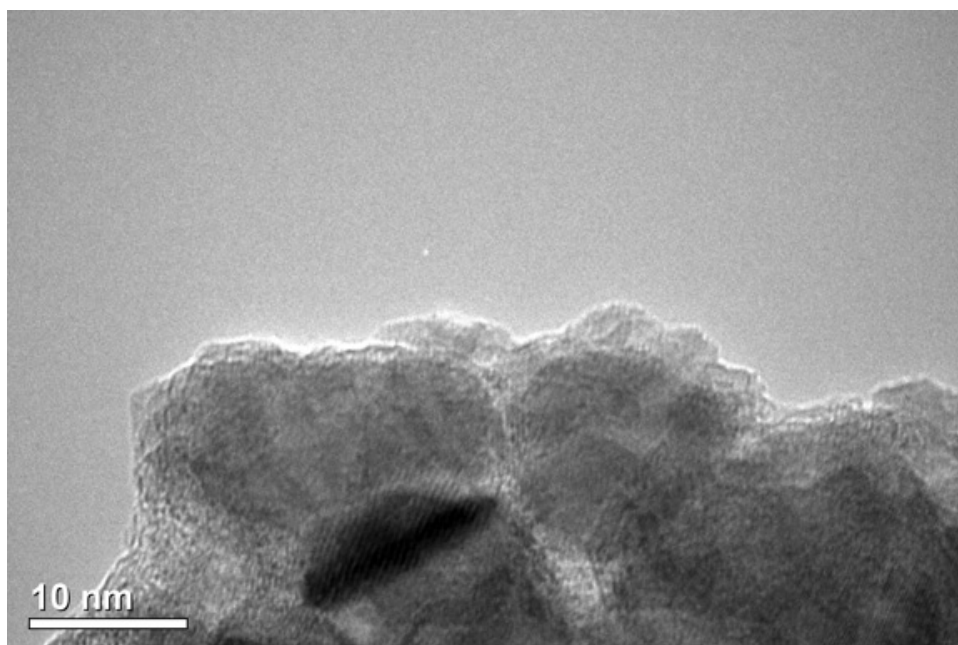
Fig. 26. (a) Bright field XTEM micrograph of $Ni_{52.5}Nb_{10}Zr_{15}Ti_{15}Pt_{7.5}$ after 1 MeV Ni^+ ion irradiation to a dose of $1x10^{16}$ cm^{-2}, region taken from that shown in Figure 25

CHAPTER VII

CONCLUSIONS

The overarching goal of the present work was to build and develop a framework for multi-scale modeling of ion-solid interactions, to understand the role of the damage cascade in this material, and to perform experiments that could lend credibility to those models. To this end a systematic approach was undertaken to develop code and perform ion irradiation experiments.

Code development resulted in a numerical method to couple together the damage cascade event, as predicted through Monte Carlo simulations, to the subsequent time dependent temperature evolution, using the finite element method. The current code SRIM, which is a staple in assessing damage cascades was linked to a code developed to model transient heat transfer, written in C++ using the dealii libraries. In order to achieve this, various methods, such as adaptive mesh refinement, SSOR, the CG method, were employed to produce a result which was numerically stable for a small spatial and temporal resolution.

The multi-scale modeling code is able to produce 2-D and 3-D time dependent temperature profiles in $Ni_{52.5}Nb_{10}Zr_{15}Ti_{15}Pt_{7.5}$ due to 1 MeV Ni^+ ion irradiation. A minimal number of inputs, such as material density, specific heat and thermal conductivity are required for code execution. The resulting output being directly accessible for visual analysis using the VisIt software.

For the case of 1 MeV Ni^+ ion irradiation in $Ni_{52.5}Nb_{10}Zr_{15}Ti_{15}Pt_{7.5}$ metallic glass, the modeling results indicate that the damage cascade is unlikely to directly induce crystallization. The cooling rate predicted by the FEM heat transfer code is 10^{14} K/s which is $\gg$ than the critical cooling rate for this material. Maximum temperatures for this configuration are approximately 5300 K. These temperatures do not persist long

and within 6 picoseconds the temperature is below the glass transition temperature of $Ni_{52.5}Nb_{10}Zr_{15}Ti_{15}Pt_{7.5}$ throughout the sample. The total time to reach steady state temperatures of 50 K in regions near the source is 20 picoseconds.

Experimental 1 MeV Ni^+ ion irradiation in $Ni_{52.5}Nb_{10}Zr_{15}Ti_{15}Pt_{7.5}$ was able to reveal interesting phenomena regarding the crystal growth and formation. Both plane view and cross-sectional TEM, HRTEM, and used to understand the crystallization mechanism and identify the phases that formed. The phases that are most likely to have formed include Ni_3Nb, Ni_3Ti and Ni_3Zr, identified using electron diffraction. STEM has revealed that due to the highly negative mixing enthalpies of Pt with Ni, Nb, and Zr, irradiation induced segregation occurs in regions that appear crystalline. To account for the results of STEM, which further indicate a high concentration of Pt in the crystal regions, it is proposed that Pt is substituting for Ni to form substitutional solid solution $(Ni,Pt)_3Nb$ and $(Ni,Pt)_3Ti$. Micrographs from the irradiated samples provides evidence that the damage cascade does not directly cause crystallization in $Ni_{52.5}Nb_{10}Zr_{15}Ti_{15}Pt_{7.5}$ metallic glass. No crystals are observed to form outside of regions of an intermediate grey precipitate phase, which differs from the nominal as=spun concentrations. This lends to a multi-stage process for crystal nucleation and growth.

REFERENCES

[1] W. Klement, F.H. Willens, and P. Duwez, "Non-crystalline structure in solidified gold-silicon alloys," *Nature*, vol. 187, pp. 869–870, September 1960.

[2] A. Inoue, "High strength bulk amorphous alloys with low critical cooling rates," *Materials Transactions, JIM*, vol. 36, no. 7, pp. 866–875, 1995.

[3] D.V. Louzguine-Luzgin, T. Shimada, and A. Inoue, "Ni-based bulk glassy alloys with large supercooled liquid region exceeding 90 K," *Intermetallics*, vol. 13, no. 11, pp. 1166–1171, 2005.

[4] A. Inoue, "Stabilization of metallic supercooled liquid and bulk amorphous alloys," *Acta Materialia*, vol. 48, pp. 279–306, 2000.

[5] F. Faupel, W. Frank, M.P. Macht, H. Mehrer, V. Naundorf, K. Ratzke, H.R. Schober, S.K. Sharma, and H. Teichler, "Diffusion in metallic glasses and supercooled melts," *Reviews of Modern Physics*, vol. 75, no. 1, pp. 237–280, Jan. 2003.

[6] A.L. Greer, K.L. Rutherford, and I.M. Hutchings, "Wear resistance of amorphous alloys and related materials," *International Materials Reviews*, vol. 47, no. 2, pp. 87–112, 2002.

[7] C.A. Pampillo, "Flow and fracture in amorphous alloys," *Journal of Materials Science*, vol. 10, pp. 1194–1227, 1975.

[8] C.A. Schuh and T.G. Nieh, "A survey of instrumented indentation studies on metallic glasses," *Journal of Materials Research*, vol. 19, no. 1, pp. 46–57, 2004.

[9] W.H. Wang, C. Dong, and C.H. Shek, "Bulk metallic glasses," *Materials Science and Engineering R*, vol. 44, pp. 45–89, 2004.

[10] W.H. Jiang, F.X. Liu, D.C. Qiao, H. Choo, and P.K. Liaw, "Plastic flow in dynamic compresion of a Zr-based bulk metallic glass," *Journal of Materials Research*, vol. 21, no. 6, pp. 1570–1575, June 2006.

[11] C. Fan and A. Inoue, "Ductility of bulk nanocrystalline composites and metallic glasses at room temperature," *Applied Physics Letters*, vol. 77, pp. 46–49, 2000.

[12] G. Xie, D.V. Louzguine-Luzgin, H. Kimura, A. Inoue, and F. Wakai, "Large-size ultrahigh strength ni-based bulk metallic glassy matrix composites with enhanced ductility fabricated by spark plasma sintering," *Applied Physics Letters*, vol. 92, no. 12, pp. 121907, 2008.

[13] J.J. Kim, Y. Choi, S. Suresh, and A.S. Argon, "Nanocrystallization during nanoindentation of a bulk amorphous metal alloy at room temperature," *Science*, vol. 295, pp. 654–657, Jan. 2002.

[14] M.L. Trudeau, J.Y. Huot, R. Schulz, D. Dussault, A. Van Neste, and G. L'Espérance, "Nanocrystalline Fe-(Co,Ni)-Si-B the mechanical crystallization of amorphous alloys and the effects on electrocatalytic reactions," *Physical Review B*, vol. 45, no. 9, pp. 4626–4636, 1992.

[15] H. Chen, Y. He, G.J. Shiflet, and S.J. Poon, "Deformation-induced nanocrystal formation in shear bands of amorphous alloys," *Nature*, vol. 367, pp. 541–543, 1994.

[16] J. Saida, M. Matsushita, and A. Inoue, "Stability of supercooled liquid and transformation behavior in Zr-based glassy alloys," *Materials Transactions*, vol.

43, no. 8, pp. 1937–1946, 2002.

[17] T. Nagase and Y. Umakoshi, "Electron irradiation induced crystallization of the amorphous phase in Zr-Cu based metallic glasses with various thermal stability," *Materials Transactions*, vol. 45, no. 1, pp. 13–23, 2004.

[18] T. Nagase, M. Nakamura, and Y. Umakoshi, "Electron irradiation induced nano-crystallization in $Zr_{66.7}Ni_{33.3}$ amorphous alloy and $Zr_{60}Al_{15}Ni_{25}$ metallic glass," *Intermetallics*, vol. 15, pp. 211–224, 2007.

[19] G. Xie, Q. Zhang, D.V. Louzguine-Luzgin, W. Zhang, and A. Inoue, "Nanocrys-tallization of $Cu_{50}Zr_{45}Ti_5$ metallic glass induced by electron irradiation," *Materials Transactions*, vol. 47, no. 8, pp. 1930–1933, 2006.

[20] E.G. Fu, J. Carter, M. Martin, G. Xie, X. Zhang, Y.Q. Wang, R. Littleton, and L. Shao, "Electron irradiation-induced structural tranformation in metallic glasses," *Scripta Materialia*, vol. 61, pp. 40–43, 2009.

[21] S. Nagata, S. Higashi, B. Tsuchiya, K. Toh, T. Shikama, K. Takahiro, K. Ozaki, K. Kawatusra, S. Yamamoto, and A. Inouye, "Ion irradiation effects on amor-phization and thermal crystallization in Zr–Al–Ni–Cu alloys," *Nuclear Instruments and Methods in Physics Research B*, vol. 257, pp. 420–423, 2007.

[22] J. Carter, E.G. Fu, M. Martin, G. Xie, X. Zhang, Y.Q. Wang, D. Wijesun-dera, X.M. Wang, W.K. Chu, S.M. McDeavitt, and L. Shao, "Ion irradiation induced nanocrystal formation in amorphous $Zr_{55}Cu_{30}Al_{10}Ni_5$ alloy," *Nuclear Instruments and Methods in Physics Research Section B: Beam Interactions with Materials and Atoms*, vol. 267, no. 17, pp. 2827–2831, 2009.

[23] P.J. Tao, Y.Z. Yang, X.J. Bai, Z.X. Mu, G.Q. Li, Z.W. Xie, and X.C. Chen,

"Study on implantation of Co ions in ZrCuAlNi bulk metallic glass," *Surface and Coatings Technology*, vol. 203, pp. 1656–1659, 2009.

[24] M. Nastasi and J.W. Mayer, "Thermodynamics and kinetics of phase transformations induced by ion irradiation," *Materials Science Reports*, vol. 6, pp. 1–51, 1991.

[25] M.H. Cohen and D. Turnbull, "Molecular transport in liquids and glasses," *The Journal of Chemical Physics*, vol. 31, no. 5, pp. 1164–1169, Nov. 1959.

[26] J.F. Ziegler, J.P. Biersack, and U. Littmark, *The Stopping and Range of Ions in Solids*, Oxford, United Kingdom: Pergamon, 1985.

[27] W. Bangerth, R. Hartmann, and G. Kanschat, "deal.II : A general-purpose object-oriented finite element library," *ACM Trans. Math. Softw.*, vol. 33, no. 4.

[28] M. Nastasi, J.W. Mayer, and J.K. Hirvonen, *Ion-Solid Interactions.*, Cambridge, Great Britain: Cambridge University Press, 1996.

[29] G.S. Was, *Fundamentals of Radiation Materials Science*, Heidelberg, Germany: Springer, 2007.

[30] O.B. Firsov, "A qualitative interpretation of the mean electron excitation energy in atomic collisions," *Sov. Phys. JETP*, vol. 36, pp. 1076, 1959.

[31] G.H. Kinchin and R.S. Pease, "The displacement of atoms in solids by radiation," *Reports on Progress in Physics*, vol. 18, pp. 1–51, 1955.

[32] J.A. Brinkman, "Production of atomic displacements by high-energy particles," *American Journal of Physics*, vol. 24, no. 4, pp. 246–267, Apr. 1956.

[33] L.C. Chen and F. Spaepen, "Calorimetric evidence for the micro-quasicrystalline structure of 'amorphous' al transition metal alloys," *Nature*, vol. 336, pp. 366–368, 1988.

[34] W.H. Wang, E. Wu, R.J. Wang, S.J. Kennedy, and A.J. Studer, "Phase transformation in a $Zr_{41}Ti_{14}Cu_{12.5}Ni_{10}Be_{22.5}$ bulk amorphous alloy upon crystallization," *Physical Review B*, vol. 66, pp. 104205, 2002.

[35] R. Busch, "The thermophysical properties of bulk metallic glass-forming liquids," *JOM*, vol. 52, no. 7, pp. 39–42, July 2000.

[36] A. Masuhr, T.A. Waniuk, R. Busch, and W.L. Johnson, "Time scales for viscous flow, atomic transport, and crystallization in the liquid and supercooled liquid states of $Zr_{41.2}Ti_{13.8}Cu_{12.5}Ni_{10.0}Be_{22.5}$," *Physical Review Letters*, vol. 82, no. 11, pp. 2290–2293, March 1999.

[37] T. Egami and Y. Waseda, "Atomic size effect on the formability of metallic glasses," *Journal of Non-Crystalline Solids*, vol. 64, pp. 113–134, 1984.

[38] Q.S. Zhang, W. Zhang, G.Q. Xie, K.S. Nakayama, H. Kimura, and A. Inoue, "Formation of bulk metallic glass in situ composites in $Cu_{50}Zr_{45}Ti_5$ alloy," *Journal of Alloys and Compounds*, vol. 431, pp. 236–240, 2007.

[39] G.Q. Xie, D.V. Louzguine-Luzgin, H. Kimura, and A. Inoue, "Nearly full density $Ni_{52.5}Nb_{10}Zr_{15}Ti_{15}Pt_{7.5}$ bulk metallic glass obtained by spark plasma sintering of gas atomized powders," *Applied Physics Letters*, vol. 90, no. 24, pp. 241902, 2007.

[40] R.B. Pond and J.M. Winter, "Calorimetric comparison of quench rates in melt spinning and melt extraction," *Materials Science and Engineering*, vol. 23, no.

2-3, pp. 87–89, 1976.

[41] R.W. Cahn and A.L. Greer, *Physical Metallurgy*, vol. 2 4th ed., Amsterdam, The Netherlands: Elsevier Science B.V., 1996.

[42] M. Iqbal, J.I. Akhter, Z.Q. Hu, H.F. Zhang, A. Qayyum, and W.S. Sun, "Mechanical properties and ion irradiation of bulk amorphous $Zr_{55}Cu_{30}Al_{10}Ni_5$ alloy," *Journal of Non-Crystalline Solids*, vol. 353, pp. 2452–2458, 2007.

[43] G. Rizza, A. Dunlop, and M. Kopcewicz, "Deformation bands in metallic glasses induced by swift heavy ions," *Nuclear Instruments and Methods in Physics Research B*, vol. 245, pp. 130–132, 2006.

[44] V. Rosato and F. Cleri, "A molecular dynamics simulation of the effects of excess free volume on the diffusion in metallic glasses," *Journal of Non-Crystalline Solids*, vol. 144, pp. 187–195, 1992.

[45] W. Frank, U. Hamlescher, H. Kronmiiller, P. Scharwaechter, and T. Schuler, "Diffusion in amorphous metallic alloys: Experiments, molecular-dynamics simulations, interpretation," *Pysica Scripta*, vol. T66, pp. 201–206, 1996.

[46] J. Carter, "Radiation induced nanocrystallization in metallic glass," Ph.D. dissertation, Texas A&M University, 2009.

[47] F. Spaepen, "A microscopic mechanism for steady state inhomogeneous flow in metallic glasses," *Acta Metallurgica*, vol. 25, pp. 407–415, 1977.

[48] Z. Yao, M.J. Caturla, and R. Schaublin, "Study of cascades damage in Ni by Md with different interatomic potentials," *Journal of Nuclear Materials*, vol. 367-370, no. Part 1, pp. 298 – 304, 2007.

[49] D.J. Bacon and Y.N. Osetsky, "Multiscale modelling of radiation damage in metals: from defect generation to material properties," *Materials Science and Engineering A*, vol. 365, no. 1-2, pp. 46 – 56, 2004.

[50] T. Diaz de la Rubia, R.S. Averback, R. Benedek, and W.E. King, "Role of thermal spikes in energetic displacement cascades," *Physical Review Letters*, vol. 59, no. 17, pp. 1930–1933, 1987.

[51] E. Balanzat, "Heavy ion induced effects in materials," *Radiation Effects and Defects in Solids*, vol. 126, pp. 97–104, 1993.

[52] L. Guan, D. Zhang, Z. Li, X. Tan, L. Li, D. Liu, R. Fang, D. Hu, and G. Liu, "Substrate temperature evolution in ions-surface interaction processes of pulsed laser deposition," *Physica B: Condensed Matter*, vol. 387, no. 1-2, pp. 194 – 202, 2007.

[53] T.E. Karakasidis and C.A. Charitidis, "Multiscale modeling in nanomaterials science," *Materials Science and Engineering: C*, vol. 27, no. 5-8, pp. 1082 – 1089, 2007.

[54] S.J. Randolph, J.D. Fowlkes, and P.D. Rack, "Effects of heat generation during electron-beam-induced deposition of nanostructures," *Journal of Applied Physics*, vol. 97, no. 12, pp. 124312, 2005.

[55] A. Caro, M. Alurralde, R. Saliba, and M. Caro, "Heat and mass transport in nanoscale phase transitions induced by collision cascades," *Journal of Nuclear Materials*, vol. 251, pp. 72 – 76, 1997.

[56] J.P. Biersack and L.G. Haggmark, "A monte carlo computer program for the transport of energetic ions in amorphous targets," *Nuclear Instruments and*

Methods, vol. 174, no. 1-2, pp. 257 – 269, 1980.

[57] Z. Chen, *Finite Element Methods and Their Applications*, Heidelberg, Germany: Springer, 2005.

[58] B.B. Sun, Y.B. Wang, J. Wen, H. Yang, M.L. Sui, J.Q. Wang, and E. Ma, "Artifacts induced in metallic glasses during tem sample preparation," *Scripta Materialia*, vol. 53, pp. 805–809, 2005.

[59] J. Als-Nielsen and D. McMorrow, *Elements of Modern X-ray Physics*, Hoboken, NJ: John Wiley and Sons, 2001.

[60] B.D. Cullity, *Elements of X-Ray Diffraction*, Reading, MA: Prentice Hall, 2001.

[61] L.D. Russell J.J. Bozzola, *Electron Microscopy: Principles and Techniques for Biologists*, Sudbury, MA: Bartlett Inc., 1999.

[62] D.B. Williams and C.B. Carter, *Transmission Electron Microscopy: A Textbook For Materials Science*, New York, NY: Plenum Press, 1996.

[63] E.G. Fu, J. Carter, M. Martin, G.Q. Xie, X. Zhang, Y.Q. Wang, R. Littleton, S. McDeavitt, and L. Shao, "Ar-ion-milling-induced structural changes of Cu50Zr45Ti5 metallic glass," *Nuclear Instruments and Methods in Physics Research Section B: Beam Interactions with Materials and Atoms*, vol. In Press, 2009.

[64] International Centre for Diffraction Data, "The powder diffraction data file", PC-PDFWIN [CD-ROM]

APPENDIX A

FINITE ELEMENT CODE

```
#include <grid/tria.h>
#include <grid/tria_boundary_lib.h>
#include <grid/grid_out.h>
#include <grid/intergrid_map.h>
#include <grid/grid_generator.h>
#include <grid/tria_accessor.h>
#include <grid/tria_iterator.h>
#include <grid/grid_refinement.h>
#include <grid/grid_tools.h>

#include <fe/fe_q.h>
#include <fe/fe_values.h>
#include <fe/mapping_q.h>

#include <dofs/dof_tools.h>
#include <dofs/dof_handler.h>
#include <dofs/dof_accessor.h>
#include <dofs/dof_constraints.h>
#include <dofs/dof_renumbering.h>

#include <base/function.h>
```

```cpp
#include <base/function_lib.h>
#include <base/function_parser.h>
#include <base/quadrature_lib.h>
#include <base/logstream.h>
#include <base/smartpointer.h>
#include <base/convergence_table.h>
#include <base/timer.h>
#include <base/thread_management.h>
#include <base/parameter_handler.h>
#include <base/utilities.h>

#include <numerics/data_out.h>
#include <numerics/vectors.h>
#include <numerics/matrices.h>
#include <numerics/error_estimator.h>
#include <numerics/solution_transfer.h>

#include <lac/vector.h>
#include <lac/full_matrix.h>
#include <lac/sparse_matrix.h>
#include <lac/solver_cg.h>
#include <lac/precondition.h>
#include <lac/identity_matrix.h>
#include <lac/sparsity_pattern.h>
#include <lac/compressed_sparsity_pattern.h>
```

```cpp
#include <fstream>

#include <iostream>

#include <cmath>

#include <typeinfo>

#include <sstream>

#include <vector>

#include <cstdlib>


#include <base/logstream.h>


using namespace dealii;


template <int dim>
class DamageCascade
{
  public:
    DamageCascade ();
    ~DamageCascade();
    void run ();


  private:
    void make_grid_and_dofs ();
    void point_sources(const MappingQ1<dim> &mapping,
        const DoFHandler<dim> &dof_handler,
        const typename DoFHandler<dim>::cell_iterator cell,
```

```cpp
                    Vector<double>& cell_rhs ,
            const unsigned int dofs_per_cell );


    void assemble_system (unsigned int timestep_number) ;
    void solve ();
    void refine_grid ();
    void output_results (unsigned int timestep_number) const;
        static void declare_parameters (ParameterHandler &prm);
        void get_parameters (ParameterHandler &prm);
        void get_points ();


    Triangulation<dim>   triangulation;
    FE_Q<dim>                       fe;
    DoFHandler<dim>       dof_handler;
    double          alpha;
    double          rhocp;
    double          delta_t;
    unsigned int           n_points;
    unsigned int           n_timesteps;
    unsigned int           timestep_number;

    std::vector<double> x;
    std::vector<double> y;
    std::vector<double> z;
    std::vector<double> t;
```

```
        std :: vector<double> energy ;


        SparsityPattern                sparsity_pattern ;
        SparseMatrix<double>           system_matrix ;
        SparseMatrix<double>           mass_matrix ;


        Vector<double>                 solution ;
        Vector<double>                 solution_old ;
        Vector<double>                 system_rhs ;
        MappingQ1<dim>                 mapping ;
        ConstraintMatrix  hanging_node_constraints ;
};



template <int dim>
DamageCascade<dim >:: DamageCascade ( )
:
fe  (1) ,
dof_handler ( triangulation ) ,
x(15429) ,
y(15429) ,
z(15429) ,
energy (15429)
{}
```

```
template <int dim>
DamageCascade<dim>::~DamageCascade()
{
        dof_handler.clear();
}


template <int dim>
void DamageCascade<dim>::make_grid_and_dofs ()
{
   dof_handler.distribute_dofs (fe);
   sparsity_pattern.reinit (dof_handler.n_dofs(),
           dof_handler.n_dofs(),
           dof_handler.max_couplings_between_dofs());


   DoFTools::make_sparsity_pattern (dof_handler, sparsity_pattern);


   sparsity_pattern.compress();
   mass_matrix.reinit(sparsity_pattern);
   solution.reinit (dof_handler.n_dofs());
   solution_old.reinit(dof_handler.n_dofs());
   system_rhs.reinit (dof_handler.n_dofs());
   hanging_node_constraints.clear ();


   DoFTools::make_hanging_node_constraints (dof_handler,
           hanging_node_constraints);
```

```
    hanging_node_constraints.close ();

    hanging_node_constraints.condense (sparsity_pattern);

    sparsity_pattern.compress();

    system_matrix.reinit (sparsity_pattern);

}
```

template <**int** dim>

void DamageCascade<dim>::declare_parameters (ParameterHandler &prm)

{

```
    prm.declare_entry ("n_points", "1",

          Patterns::Integer (),

          "Number_of_points_where_we_have_an_quantity_of_interest");
    prm.declare_entry ("n_timesteps", "1",

          Patterns::List (Patterns::Double()),

          "The_number_of_time_steps_in_the_problem");
    prm.declare_entry ("delta_t", "1",

          Patterns::Double (),

          "This_is_the_timestep_of_the_problem");
    prm.declare_entry ("Rho_Cp", "1",

          Patterns::List (Patterns::Double()),

          "Constants_associated_with_the_bulk");
    prm.declare_entry ("Alpha", "1",

          Patterns::List (Patterns::Double()),

          "The_diffussivity_associated_with_the_bulk");
```

```
}


template <int dim>
void DamageCascade<dim>::get_parameters (ParameterHandler &prm)
{
  n_points = prm.get_integer ("n_points");
  n_timesteps = prm.get_double ("n_timesteps");
  delta_t = prm.get_double ("delta_t");
  rhocp = prm.get_double ("Rho_Cp");
  alpha = prm.get_double ("Alpha");
}


template <int dim>
void DamageCascade<dim>::get_points ()
{
  const std::string filename =  "COL_EDIT.txt";
  std::ifstream inPoint (filename.c_str ());
  if (!inPoint)
  {
    std::cerr << "File could not be opened." << std::endl;
    std::exit (1);
  }
  for (int i=0; i<n_points; i++)
  {
    inPoint >> energy[i] >> x[i] >> y[i] >> z[i];
```

```
  }
  inPoint.close();


  for(int i=0; i<n_points; i++)
  {
    energy[i] = energy[i] * (1.6022E-19) * (10E25) * (1E-12);
    x[i] = x[i] * 1E-10;
    y[i] = y[i] * 1E-10;
    z[i] = z[i] * 1E-10;
  }
}


template<int dim>
void DamageCascade<dim>::point_sources
(const MappingQ1<dim>&mapping,
const DoFHandler<dim> &dof_handler,
const typename DoFHandler<dim>::cell_iterator cell,
Vector<double>& cell_rhs,
const unsigned int dofs_per_cell)
{
  for(unsigned int i_point=0; i_point < n_points; i_point++)
  {
    Point<dim> r_0(x[i_point], y[i_point], z[i_point]);
    double eps = 1E-16;
    Point<dim> vertex_0 (cell->vertex(0)(0),
```

```
                                                cell->vertex(0)(1),
                                                cell->vertex(0)(2));
Point<dim> vertex_1 (cell->vertex(1)(0),
                                      cell->vertex(1)(1),
                                      cell->vertex(1)(2));
Point<dim> vertex_2 (cell->vertex(2)(0),
                                      cell->vertex(2)(1),
                                      cell->vertex(2)(2));
Point<dim> vertex_3 (cell->vertex(3)(0),
                                      cell->vertex(3)(1),
                                      cell->vertex(3)(2));
Point<dim> vertex_4 (cell->vertex(4)(0),
                                      cell->vertex(4)(1),
                                      cell->vertex(4)(2));
Point<dim> vertex_5 (cell->vertex(5)(0),
                                      cell->vertex(5)(1),
                                      cell->vertex(5)(2));
Point<dim> vertex_6 (cell->vertex(6)(0),
                                      cell->vertex(6)(1),
                                      cell->vertex(6)(2));
Point<dim> vertex_7 (cell->vertex(7)(0),
                                      cell->vertex(7)(1),
                                      cell->vertex(7)(2));


if(r_0(0) >= (vertex_0(0) + eps*cell->diameter()) &&
```

```
r_0(1) >= (vertex_0(1) + eps*cell->diameter()) &&

r_0(2) >= (vertex_0(2) + eps*cell->diameter()) &&

r_0(0) <= (vertex_7(0) - eps*cell->diameter()) &&

r_0(1) <= (vertex_7(1) - eps*cell->diameter()) &&

r_0(2) <= (vertex_7(2) - eps*cell->diameter()))

{

  const std::pair<typename DoFHandler<dim>::
          active_cell_iterator, Point<dim> >
  cell_point = GridTools::
          find_active_cell_around_point (mapping,
          dof_handler, r_0);
  Assert(GeometryInfo<dim>::
          distance_to_unit_cell(cell_point.second)
          < 1e-10, ExcInternalError());
  const Quadrature<dim> quadrature (GeometryInfo<dim>::
          project_to_unit_cell(cell_point.second));
  FEValues<dim> r_0_fe_values (mapping,
          fe, quadrature, update_values | update_gradients);
  r_0_fe_values.reinit(cell_point.first);


  for(unsigned int i=0; i<dofs_per_cell; ++i)
  cell_rhs(i) +=.5 * energy[i_point] * (1/rhocp) *
    r_0_fe_values.shape_value(i,0);
    }
    if((r_0(0) <=(vertex_0(0)+eps*cell->diameter())) &&
```

```
        (r_0(0) >= (vertex_0(0)-eps*cell->diameter())))
{
if ((r_0(1) >= vertex_0(1) + eps*cell->diameter()) &&
    (r_0(1) <= vertex_2(1) - eps*cell->diameter()))
{
if ((r_0(2) >= vertex_0(2) + eps*cell->diameter()) &&
    (r_0(2) <= vertex_4(2) - eps*cell->diameter()))
{
const std::pair<typename DoFHandler<dim>::
        active_cell_iterator, Point<dim> >
cell_point = GridTools::
        find_active_cell_around_point (mapping,
        dof_handler, r_0);
Assert(GeometryInfo<dim>::
        distance_to_unit_cell(cell_point.second)
        < 1e-10, ExcInternalError());
const Quadrature<dim> quadrature (GeometryInfo<dim>::
        project_to_unit_cell(cell_point.second));
FEValues<dim> r_0_fe_values(mapping,
        fe, quadrature, update_values | update_gradients);
r_0_fe_values.reinit(cell_point.first);

for(unsigned int i=0; i<dofs_per_cell; ++i)
cell_rhs(i) +=.5 * energy[i_point] * (1/rhocp) *
    r_0_fe_values.shape_value(i,0)/2.0;
```

```
        }
        if ((( r_0 (2) >= ( vertex_0 (2)-eps*cell ->diameter ()))&&
           ( r_0 (2) <= ( vertex_0 (2)-eps*cell ->diameter ())))  ||
           (( r_0 (2) >= ( vertex_4 (2)-eps*cell ->diameter ()))&&
           ( r_0 (2) <= ( vertex_4 (2)-eps*cell ->diameter ())))))
        {
        const std :: pair<typename DoFHandler<dim >::
               active_cell_iterator , Point<dim> >
        cell_point = GridTools ::
               find_active_cell_around_point (mapping ,
               dof_handler , r_0 );
        Assert (GeometryInfo<dim >::
               distance_to_unit_cell ( cell_point . second )
               < 1e-10, ExcInternalError ());
        const Quadrature<dim> quadrature (GeometryInfo<dim >::
               project_to_unit_cell ( cell_point . second ));
        FEValues<dim> r_0_fe_values (mapping ,
               fe , quadrature , update_values | update_gradients );
        r_0_fe_values . reinit ( cell_point . first );

        for(unsigned int i=0; i<dofs_per_cell; ++i)
        cell_rhs (i) +=         .5 * energy [ i_point ] * (1/rhocp) *
           r_0_fe_values . shape_value (i ,0)  /4.0 ;
        }
}
```

```
if  (((r_0(1) <= vertex_0(1) + eps*cell->diameter()) &&
     (r_0(1) >= vertex_0(1)) &&
     (r_0(2) <= vertex_0(2) + eps*cell->diameter()) &&
     (r_0(2) >= vertex_0(2))) ||
     ((r_0(1) <= vertex_2(1) + eps*cell->diameter()) &&
     (r_0(1) >= vertex_2(1)) &&
     (r_0(2) <= vertex_2(2) + eps*cell->diameter()) &&
     (r_0(2) >= vertex_2(2))) ||
     ((r_0(1) <= vertex_4(1) + eps*cell->diameter()) &&
     (r_0(1) >= vertex_4(1)) &&
     (r_0(2) <= vertex_4(2) + eps*cell->diameter()) &&
     (r_0(2) >= vertex_4(2))) ||
     ((r_0(1) <= vertex_6(1) + eps*cell->diameter()) &&
     (r_0(1) >= vertex_6(1)) &&
     (r_0(2) <= vertex_6(2) + eps*cell->diameter()) &&
     (r_0(2) >= vertex_6(2))))
{
const std::pair<typename DoFHandler<dim>::
        active_cell_iterator, Point<dim> >
cell_point = GridTools::
        find_active_cell_around_point (mapping,
        dof_handler, r_0);
Assert(GeometryInfo<dim>::
        distance_to_unit_cell(cell_point.second)
        < 1e-10, ExcInternalError());
```

```
const Quadrature<dim> quadrature (GeometryInfo<dim>::
        project_to_unit_cell(cell_point.second));
FEValues<dim> r_0_fe_values(mapping,
        fe, quadrature, update_values | update_gradients);
r_0_fe_values.reinit(cell_point.first);


for(unsigned int i=0; i<dofs_per_cell; ++i)
cell_rhs(i) +=  .5 * energy[i_point] * (1/rhocp) *
r_0_fe_values.shape_value(i,0) / 8.0 ;
}
}
if((r_0(0) <=(vertex_1(0)+eps*cell->diameter())) &&
  (r_0(0) >= (vertex_1(0)-eps*cell->diameter()))))
{
if ((r_0(1) >= vertex_1(1) + eps*cell->diameter()) &&
  (r_0(1) <= vertex_3(1) - eps*cell->diameter()))
{
if ((r_0(2) >= vertex_1(2) + eps*cell->diameter()) &&
  (r_0(2) <= vertex_5(2) - eps*cell->diameter()))
{
const std::pair<typename DoFHandler<dim>::
        active_cell_iterator, Point<dim> >
cell_point = GridTools::
        find_active_cell_around_point (mapping,
        dof_handler, r_0);
```

```
Assert ( GeometryInfo<dim>::

            distance_to_unit_cell ( cell_point . second )

            < 1e-10, ExcInternalError ());
    const Quadrature<dim> quadrature ( GeometryInfo<dim>::

            project_to_unit_cell ( cell_point . second ));
    FEValues<dim> r_0_fe_values ( mapping ,

            fe , quadrature , update_values | update_gradients );
    r_0_fe_values . reinit ( cell_point . first );


    for ( unsigned int i =0; i<dofs_per_cell ; ++i )
    cell_rhs ( i ) +=.5 * energy [ i_point ] * (1/rhocp) *
       r_0_fe_values . shape_value ( i ,0) / 2.0 ;
}
if ((( r_0 (2) >= ( vertex_1 (2) - eps*cell ->diameter ()))&&
   ( r_0 (2) <= ( vertex_1 (2) - eps*cell ->diameter ())))  ||
   (( r_0 (2) >= ( vertex_5 (2) - eps*cell ->diameter ()))&&
   ( r_0 (2) <= ( vertex_5 (2) - eps*cell ->diameter ()))))
{
const std :: pair<typename DoFHandler<dim>::

            active_cell_iterator , Point<dim> >
cell_point = GridTools ::

            find_active_cell_around_point ( mapping ,

            dof_handler , r_0 );
Assert ( GeometryInfo<dim>::

            distance_to_unit_cell ( cell_point . second )
```

```
                    < 1e-10, ExcInternalError());
const Quadrature<dim> quadrature (GeometryInfo<dim>::
              project_to_unit_cell(cell_point.second));
FEValues<dim> r_0_fe_values(mapping,
            fe, quadrature, update_values | update_gradients);
r_0_fe_values.reinit(cell_point.first);


for(unsigned int i=0; i<dofs_per_cell; ++i)
  cell_rhs(i) +=.5 * energy[i_point] * (1/rhocp) *
    r_0_fe_values.shape_value(i,0) / 4.0 ;

  }

}
if ((((r_0(1) <= vertex_1(1) + eps*cell->diameter()) &&
  (r_0(1) >= vertex_1(1)) &&
  (r_0(2) <= vertex_1(2) + eps*cell->diameter()) &&
  (r_0(2) >= vertex_1(2))) ||
  ((r_0(1) <= vertex_3(1) + eps*cell->diameter()) &&
  (r_0(1) >= vertex_3(1)) &&
  (r_0(2) <= vertex_3(2) + eps*cell->diameter()) &&
  (r_0(2) >= vertex_3(2))) ||
  ((r_0(1) <= vertex_5(1) + eps*cell->diameter()) &&
  (r_0(1) >= vertex_5(1)) &&
  (r_0(2) <= vertex_5(2) + eps*cell->diameter()) &&
  (r_0(2) >= vertex_5(2))) ||
  ((r_0(1) <= vertex_7(1) + eps*cell->diameter()) &&
```

```
(r_0(1) >= vertex_7(1)) &&

(r_0(2) <= vertex_7(2) + eps*cell->diameter()) &&

(r_0(2) >= vertex_7(2)))))

{

const std::pair<typename DoFHandler<dim>::

        active_cell_iterator, Point<dim> >

cell_point = GridTools::

        find_active_cell_around_point (mapping,

        dof_handler, r_0);

Assert(GeometryInfo<dim>::

        distance_to_unit_cell(cell_point.second)

        < 1e-10, ExcInternalError());

const Quadrature<dim> quadrature (GeometryInfo<dim>::

        project_to_unit_cell(cell_point.second));

FEValues<dim> r_0_fe_values(mapping,

        fe, quadrature, update_values | update_gradients);

r_0_fe_values.reinit(cell_point.first);


for(unsigned int i=0; i<dofs_per_cell; ++i)

  cell_rhs(i) +=.5 * energy[i_point] * (1/rhocp)

  * r_0_fe_values.shape_value(i,0) / 8.0 ;

  }

 }

}

}
```

```cpp
}
template <int dim>
void DamageCascade<dim>::assemble_system
(unsigned int timestep_number)
{
  QGauss<dim> quadrature_formula(2);
  FEValues<dim> fe_values (fe, quadrature_formula,
    update_values | update_gradients |
    update_q_points | update_JxW_values);
  const unsigned int dofs_per_cell = fe.dofs_per_cell;
  const unsigned int n_q_points
  = quadrature_formula.n_quadrature_points;
  FullMatrix<double>     cell_matrix (dofs_per_cell,
   dofs_per_cell);
  FullMatrix<double>     cell_mass_matrix (dofs_per_cell,
   dofs_per_cell);
  Vector<double> cell_rhs (dofs_per_cell);
  std::vector<unsigned int> local_dof_indices (dofs_per_cell);
  typename DoFHandler<dim>::active_cell_iterator
  cell = dof_handler.begin_active(),
  endc = dof_handler.end();
  for (; cell!=endc; ++cell)
  {
    fe_values.reinit (cell);
    cell_matrix = 0;
```

```
cell_rhs = 0;

std::vector<double> T_value;

T_value.resize(n_q_points);

fe_values.get_function_values(solution_old, T_value);

for (unsigned int q_point=0; q_point<n_q_points; ++q_point)

  for (unsigned int i=0; i<dofs_per_cell; ++i)

  {

    for (unsigned int j=0; j<dofs_per_cell; ++j)

    {

    cell_matrix(i,j) += (( .5 * alpha *

    fe_values.shape_grad (i, q_point) *

      fe_values.shape_grad (j, q_point) +

      ( (1/delta_t) * fe_values.shape_value (i, q_point) *

      fe_values.shape_value (j, q_point))) *

      fe_values.JxW (q_point));


      cell_rhs(i) += (( -.5 * alpha *

      fe_values.shape_grad (i, q_point) *

        fe_values.shape_grad (j, q_point) * T_value[q_point] +

        ( (1/delta_t) *fe_values.shape_value (i, q_point) *

        fe_values.shape_value (j, q_point) * T_value[q_point])) *

        fe_values.JxW (q_point));

    }

  }

if (timestep_number<=2)
```

```
  {
    point_sources(mapping,
        dof_handler, cell, cell_rhs, dofs_per_cell);
  }


  cell->get_dof_indices (local_dof_indices);
  for (unsigned int i=0; i<dofs_per_cell; ++i)
  {
    for (unsigned int j=0; j<dofs_per_cell; ++j)
    {
      system_matrix.add (local_dof_indices[i],
          local_dof_indices[j],
          cell_matrix(i,j));
    }


    system_rhs(local_dof_indices[i]) += cell_rhs(i);
  }
}


hanging_node_constraints.condense (system_matrix);
hanging_node_constraints.condense (system_rhs);
std::map<unsigned int,double> boundary_values;
VectorTools::interpolate_boundary_values (dof_handler,
  0,
  ConstantFunction<dim>(0),
```

```
      boundary_values );
    MatrixTools :: apply_boundary_values ( boundary_values ,
        system_matrix ,
        solution ,
        system_rhs );
}


template <int dim>
void DamageCascade<dim >:: solve ()
{
    SolverControl solver_control (5000, 1e-12);
    SolverCG<> cg (solver_control );
    PreconditionSSOR<> preconditioner ;
    preconditioner . initialize (system_matrix, 1.2);
    cg.solve (system_matrix, solution, system_rhs ,
        PreconditionIdentity ());
    hanging_node_constraints . distribute (solution );
}
template <int dim>


void DamageCascade<dim >:: refine_grid ()
{
    Vector<float> estimated_error_per_cell
            (triangulation . n_active_cells ());
```

```
    KellyErrorEstimator<dim>::estimate (dof_handler,
      QGauss<dim-1>(2),
      typename FunctionMap<dim>::type(),
      solution,
      estimated_error_per_cell);
    GridRefinement::
          refine_and_coarsen_fixed_number (triangulation,
          estimated_error_per_cell, 0.4, 0.08);
    triangulation.execute_coarsening_and_refinement ();
}
template <int dim>
void DamageCascade<dim>::
        output_results (unsigned int timestep_number) const
{
  DataOut<dim> data_out;
  data_out.attach_dof_handler (dof_handler);
  data_out.add_data_vector (solution, "solution");
  data_out.build_patches ();
  const unsigned int j = timestep_number;
  const std::string filename = "solution-" +
    Utilities::int_to_string (j, 6) + ".vtk";
  std::ofstream output (filename.c_str());
  data_out.write_vtk (output);
}
template <int dim>
```

```
void DamageCascade<dim>::run ()

{

  const Point<dim> left = Point<dim>(-100E-9,-300E-9,-500E-9);

  const Point<dim> right = Point<dim>(500E-9,300E-9,500E-9);

  GridGenerator::hyper_rectangle (triangulation,

    right,

    left,

    false);

  triangulation.refine_global (1);

  make_grid_and_dofs();

  ParameterHandler parameter_handler;

  declare_parameters (parameter_handler);

  parameter_handler.read_input ("project.prm");

  get_parameters (parameter_handler);

  get_points ();


  solution_old.reinit(dof_handler.n_dofs());

  for ( unsigned int i = 0; i < dof_handler.n_dofs(); i++)

  {

    solution_old(i)= 0;

  }

  solution=solution_old;

  for (unsigned int timestep_number=1;

    timestep_number<=n_timesteps;

    ++timestep_number)
```

```
  {
    std :: cout <<" Solving _Time _Step _"<< timestep_number << std :: endl ;
    assemble_system ( timestep_number ) ;
    solve ();
    if ( timestep_number == 1)
    {
      for ( unsigned int j = 1; j < 8; j++)
      {
        refine_grid ();
        make_grid_and_dofs ();
        assemble_system ( timestep_number );
        solve ();
      }
    }
    else
    {
      assemble_system ( timestep_number );
      solve ();
    }
  solution_old=solution ;
  output_results ( timestep_number );
  }
}
int main ()
{
```

```
deallog.depth_console (0);
const unsigned int dim=3;
{
DamageCascade<dim> damage_cascade;
damage_cascade.run ();
}
return 0;
}
```

VITA

Name:	Michael Thomas Myers
Address:	Department of Nuclear Engineering
	Texas A&M University
	134D Zachry Engineering Center
	College Station, TX 77843-3133
Email:	myers.651@tamu.edu
Education:	B.S., Engineering Physics, The Ohio State University, 2007
	M.S., Nuclear Engineering, Texas A&M University, 2010
Professional:	Engineer, Core Engineering, Westinghouse Electric Co., 2007-08

The typist for this thesis was the author.